Fall 2013

Fiber inline pressure and acoustic sensor fabricated with femtosecond laser

Yinan Zhang

Department: Electrical and Computer Engineering

FIBER INLINE PRESSURE AND ACOUSTIC SENSOR FABRICATED WITH FEMTOSECOND LASER

by

YINAN ZHANG

A DISSERTATION

Presented to the Faculty of the Graduate School of the

MISSOURI UNIVERSITY OF SCIENCE & TECHNOLOGY

In Partial Fulfillment of the Requirements for the Degree

DOCTOR OF PHILOSOPHY

in

ELECTRICAL ENGINEERING

2013

Approved by

Dr. Hai Xiao, Advisor
Dr. Jun Fan
Dr. Chang-Soo Kim
Dr. Hai-Lung Tsai
Dr. Randy H. Moss

ABSTRACT

Pressure and acoustic measurements are required in many industrial applications such as down-hole oil well monitoring, structural heath monitoring, engine monitoring, study of aerodynamics, etc. Conventional sensors are difficult to apply due to the high temperature, electromagnetic-interference noise and limited space in such environments. Fiber optic sensors have been developed since the last century and have proved themselves good candidates in such harsh environment.

This dissertation aims to design, develop and demonstrate miniaturized fiber pressure/acoustic sensors for harsh environment applications through femtosecond laser fabrication. Working towards this objective, the dissertation explored two types of fiber inline microsensors fabricated by femtosecond laser: an extrinsic Fabry-Perot interferometric (EFPI) sensor with silica diaphragm for pressure/acoustic sensing, and an intrinisic Fabry-Perot interferometer (IFPI) for temperature sensing. The scope of the dissertation work consists of device design, device modeling/simulation, laser fabrication system setups, signal processing method development and sensor performance evaluation and demonstration.

This research work provides theoretical and experimental evidences that the femtosecond laser fabrication technique is a valid tool to fabricate miniaturized fiber optic pressure and temperature sensors which possess advantages over currently developed sensors.

ACKNOWLEDGMENTS

I would like to take this opportunity to thank all those people who helped me with the successful completion of my research. First, I would like to express my gratitude to my advisor Dr. Hai Xiao, without who this research could be considered incomplete. I thank him for giving me a chance to work with him and for his continued support with valuable advice and encouragement. His subtle guidance with unbelievable patience has made a great impact on this research and me.

I am grateful to Dr. Jun Fan, Dr. Randy H. Moss, Dr. Chang-Soo Kim, and Dr. Hai-Lung Tsai, for their very well organized classes, which cultivated my interest in study and inspired my research work. Also, I am much honored to have them as my committee members.

Additional gratitude is owed to all the members and alumni from Dr. Xiao's research group. I am very happy to work with everybody during my stay in this lab. Many thanks should go to my lab mates: Xinwei Lan, Tao Wei, Ying Huang, Hongbiao Duan, Xia Fang, Baokai Cheng, Sudha Sneha Devarakonta, Jie Huang, Lei Yuan, Hanzheng Wang, Amardeep Kaur, Ahmed Khan Tameem, Mujahid Abdul, Saba Khan Adviya, Yang Song, Wenge Zhu, Li Kang, Yanjun Li, Qun Han, Xiaoyan Wen, Jie Liu, Smith Kenny, Edward Pienkowski, Xinyao Guo, Xinyun Guo and Zhan Gao.

I thank my parents for everything they have done for me and I am happy that they agree to participate in my commencement all the way from the opposite of the earth.

Finally, I would like to thank the sponsors for this project. They are the U.S. Department of Energy through the National Energy Technology program.

TABLE OF CONTENTS

LIST OF ILLUSTRATIONS

Page

LIST OF TABLES

Page

1. INTRODUCTION

This section presents a general introduction of the dissertation work. A brief review of the current state-of-the-art pressure/acoustic sensing technologies and the application areas is provided. The challenges, limitations and unsolved issues are summarized. Consequently, the research objectives and the scientific /technical topics to be addressed by this dissertation are derived. After a brief description of the scope of the dissertation work, the research innovations are summarized in the context of design, development and demonstration of novel sensors fabricated by femtosecond laser.

1.1. PRESSURE MEASUREMENT FUNDAMENTALS

Pressure is force per unit area applied in a direction perpendicular to the surface of an object. Pressure is measured in any unit of force divided by any unit of area. The SI unit of pressure is (the Newton per square meter), which is called the Pascal (Pa) after the seventeenth-century philosopher and scientist Blaise Pascal. A pressure of 1 Pa is small; it approximately equals the pressure exerted by a dollar bill resting flat on a table [1].

Sound pressure or acoustic pressure is the local pressure deviation from the ambient atmospheric pressure, caused by a sound wave. In air, sound pressure can be measured using a microphone, and in water with a hydrophone.

There are three methods for measuring pressure: absolute, gauge, and differential [2]. Absolute pressure is referenced to the pressure in a vacuum, whereas gauge and differential pressures are referenced to another pressure such as the ambient atmospheric pressure or pressure in an adjacent vessel.

1.1.1. Absolute Pressure. The absolute measurement method is relative to 0 Pa, the static pressure in a vacuum. The pressure being measured is being acted upon by atmospheric pressure in addition to the pressure of interest. Therefore, absolute pressure measurement includes the effects of atmospheric pressure. This type of measurement is well-suited for atmospheric pressures such as those used in altimeters or vacuum pressures.

1.1.2. Gauge Pressure. Gauge and differential measurement methods are relative to some other dynamic pressure. In the gauge method, the reference is the ambient atmospheric pressure. This means that both the reference and the pressure of interest are acted upon by atmospheric pressure. These types of measurements are easy to identify in examples such as tire pressure and blood pressure measurements.

1.1.3. Differential Pressure. Differential pressure is very similar to gauge pressure; however, the reference is another pressure point in the system rather than the ambient pressure. You can use this method to maintain a relative pressure between two vessels such as compressor tank and associated feed line.

1.2. PRESSURE MEASUREMENT TECHNIQUES

1.2.1. Manometer. Manometer is an instrument that uses a column of liquid to measure pressure, although the term is often used nowadays to mean any pressure measuring instrument. It is based on the hydrostatic balance principle which means the pressure at any point in a hydrostatic fluid is just due to the weight of the overlying fluid.

1.2.2. Vacuum Gauge. A vacuum gauge is used to measure the pressure in a vacuum—which is further divided into two subcategories, high and low vacuum (and sometimes ultra-high vacuum). The applicable pressure range of many of the techniques used to measure vacuums has an overlap. Hence, by combining several different types of gauge, it is possible to measure system pressure continuously from 1000 mbar down to 10−11 mbar.

1.2.3. Mechanical Pressure Gauge. The first pressure gauge uses flexible elements as sensors. As pressure changed, the flexible element moved, and this motion was used to rotate a pointer in front of a dial. In these mechanical pressure sensors, a Bourdon tube, a diaphragm, or a bellows element detected the process pressure and caused a corresponding movement. A Bourdon tube is C-shaped and has an oval cross-section with one end of the tube connected to the process pressure. The other end is sealed and connected to the pointer or transmitter mechanism. To increase their sensitivity, Bourdon tube elements can be extended into spirals or helical coils. This

increases their effective angular length and therefore increases the movement at their tip, which in turn increases the resolution of the transducer.

The family of flexible pressure sensor elements also includes the bellows and the diaphragms. Diaphragms are popular because they require less space and because the motion (or force) they produce are sufficient for operating electronic transducers. They also are available in a wide range of materials for corrosive service applications.

1.2.4. MEMS Pressure Sensor. Microelectromechanical systems (MEMS) is the technology of very small devices. MEMS devices generally range in size from 20 micrometers (20 millionths of a meter) to a millimeter (i.e. 0.02 to 1.0 mm). They usually consist of a central unit that processes data (the microprocessor) and several components that interact with the surroundings such as microsensors. MEMS broaden the fabrication approaches developed for the integrated circuit industry to include mechanical elements for instance beams, gears, diaphragms and springs to devices [3].

MEMS pressure sensors have been developed recently [4-7]. They can be categorized into two types, piezoresistive and capacitive sensors, based on their sensing mechanisms.

1.2.4.1 Piezoresistive sensors. Piezoresistive pressure sensors are one of the very first products of MEMS technology. Those products are widely used in biomedical applications, automotive industry and household appliances. The sensing material in a piezoresistive pressure sensor is a diaphragm formed on a silicon substrate, which bends with applied pressure. A deformation occurs in the crystal lattice of the diaphragm because of that bending. This deformation causes a change in the band structure of the piezoresistors that are placed on the diaphragm, leading to a change in the resistivity of the material. This change can be an increase or a decrease according to the orientation of the resistors. The resistors can be connected in a Wheatstone bridge. The readout of pressure is read from the output of the Wheatstone bridge circuit.

Piezoresistive sensors are widely used as commercial MEMS pressure sensors. They have very good linearity to pressure change. However, as resistivity of sensing material is a function of ambient temperature, the output of piezoresitive sensor is affected by temperature change, and they usually consume a lot of power.

1.2.4.2 Capacitive sensors. Capacitive pressure sensor is another type of MEMS pressure sensor. The pressure sensing part is a pair of parallel plates that form a capacitor. One plate is fixed to a sensing membrane which deforms under pressure, and the other plate is attached to a substrate which is insensitive to pressure change. When pressure is applied to the membrane, its deformation will result in a change of capacitance. The capacitor is connected to an electrical circuit which converts the capacitance to a voltage or frequency signal as the sensor output.

Compared with piezoresistive pressure sensors, the capacitive sensors can operate in higher temperatures with low temperature coefficient, and they consume less power in operation.

MEMS pressure sensors have advantages of low cost, high sensitivity and suitable for mass production. Companies such as GE and Freescale Semiconductor are developing MEMS sensors for many years, providing high performance MEMS pressure sensors. However, MEMS sensors are not suitable for harsh environment applications. First, MEMS sensors are fabricated with silicon material which is limited to operate at temperatures lower than 150°. Second, as MEMS sensors usually include multiple materials with different coefficients of thermo-expansion (CTE). Third, MEMS sensors are subject to electromagnetic interference (EMI).

1.2.5. Fiber Optic Pressure Sensor. Fiber optic sensors can be used to measure pressure, and many different types of fiber optic pressure sensors have been developed. These include intensity based fiber optic sensors, interferometric fiber optic sensors and polarization modulated fiber optic sensors.

1.2.5.1 Intensity based sensors. Intensity modulation induced by micro bending in multimode fibers is considered as a transduction mechanism for detecting environmental changes such as pressure, temperature, acceleration, magnetic and electric fields [8]. It is one of the earliest fiber optic sensors. The microbend is carried by spatial variations in the layer of optical fiber, which induces coupling between the modes of the fiber. Some of the coupling is to radiative modes. When a periodic microbend is induced along the fiber axis, light is coupled between the modes, and power transfer takes place.

1.2.5.2 Polarization modulated pressure sensors. Two types of polarization modulated pressure sensor have been developed, based on the Faraday Effect and photoelastic effect, and the latter is mostly used. Photoelastic effect converts applied pressure to polarization state change in a fiber. Since Spillman demonstrated the first fiber optic pressure sensor on photoelastic effect in 1982 [9], various photoelastic fiber pressure sensors have been fabricated, such as embedded pressure sensor based on polarization maintaining photonic crystal fiber [10].

1.2.5.3 Interferometric pressure sensors. Four types of interferometric fiber pressure sensors have been developed so far, namely Michelson interferometer (MI), Mach-Zehnder interferometer (MZI), Fabry Perot interferometer (FPI) and Sagnac interferometers (SI). For MZI, MI and SI, the incident light is split into two arms by a fiber splitter and then recombined by a fiber combiner. For Fabry-Perot interferometers (FPIs), two parallel separated mirrors are required to partially reflect the lead-in optical signals [11].

Optical fiber Sagnac interferometers have been developed for gyroscopes and other sensor applications due to their unique advantages, such as simple design, ease of manufacture, and lower susceptibility to environmental pickup noise in comparison to other types of fiber optic sensors. Polarization-maintaining fiber (PMF) is usually used in Sagnac interferometers to introduce optical path difference and cause interference between the two counter propagating waves in the fiber loop. Recently, fiber Sagnac interferometer pressure sensor realized by using a polarization maintaining photonic-crystal fiber (PM-PCF) as the sensing element has been proposed and demonstrated[12, 13].

Michelson and Mach-Zehnder interferometer are investigated in early years for pressure measurement. For example, a Michelson fiber optic pressure sensor with electro-optic feedback system for remote fluid pressure measurements [14] and imbalanced Mach-Zehnder interferometer integrated in micromachined silicon substrate for pressure sensor [15]. The path difference induced by the pressure leads to interference spectrum shift; however, due to the very low stress-optic coefficient of fused silica, a very long length of sensing fiber is required to achieve the desirable sensitivity. On the other hand, Michelson and Mach-Zehnder interferometer sensors fabricated with conventional non

polarization-preserving fibers are subject to polarization fading caused by temperature variations and minor positional changes in the sensor [16].

Fabry Perot interferometer consists of two partial reflection mirrors that form a cavity. Incident light entering the Fabry Perot interferometer will have multiple reflections between the mirrors. Fiber optic Fabry Perot interferometer can be categorized into two types: intrinsic Fabry Perot interferometer (IFPI) and extrinsic Fabry Perot interferometer (EFPI). In IFPI, the Fabry Perot cavity is formed by a section of fiber with its two ends partially reflective, by coating or other method. In EFPI, the Fabry Perot cavity is filled with another material instead of fiber, i.e., air, fluid, etc.
In IFPI, the interference signal is a function of cavity length, the refractive index of the fiber, and the reflectivity of the interface. By modulating the above parameters, such as refractive index as a function of temperature, IFPI can be used for temperature sensing. It can also be used for strain sensing, etc.

Fiber optic EFPI has been developed into pressure sensors. Compared with Sagnac, Mach-Zehnder and Michelson interferometers, EFPI pressure sensor has advantages such as high sensitivity, short sensing fiber length, simple structure, independence of polarization fading, etc. The development of EFPI pressure sensors will be discussed in the next section.

1.3. MOTIVATIONS AND OBJECTIVES

Applications and Motivations: This research was initially motivated by developing novel sensor for pressure/acoustic measurement in harsh environment industrial applications, for example, down-hole pressure and temperature monitoring [11], partial discharge detection in transformers [17], in-cylinder pressure monitoring in engines [18], study of aerodynamics [19], embedded ultrasound detection [20], etc. Acquiring accurate pressure measurements in these harsh environments has always challenged the available measurement technology. The motivation of this research is to meet the recent increasing needs for optical fiber pressure sensors capable of operating accurately and reliably in these harsh environments.

There exist a number of important considerations for sensors targeting such applications. First, the sensor needs to survive the harsh environment. For example, pressure monitoring in many cases is required to operate at temperatures higher than 500 °C. As such, the sensors need to survive the high temperature conditions and have a low temperature cross sensitivity. Cross-sensitivity, especially the temperature cross-sensitivity, could result in large amount of measurement error induced by changes in environmental parameters other than the one to be measured. In most cases, more than one adverse parameter can be found in a typical harsh environment. For example, in a combustion engine, high temperature and high pressure coexist at the same time. In this case, a pressure sensor for engine monitoring should have zero response to temperature change.

In addition, pressure measurement sometimes needs to be performed in aqueous environments where the types and concentrations of the liquids may vary dramatically. Therefore, a good pressure sensor is also required to be insensitive to the changes in ambient media.

Acoustic characterization of medical ultrasound devices is needed for optimization of image quality in diagnostic applications and to ensure their safety and effectiveness in therapeutic applications [21]. Current medical diagnostic ultrasound systems usually employ center frequencies ranging from ~2 MHz to 20 MHz. In the past decades, therapeutic applications of ultrasound have experienced fast growth. The majority of the commercially available devices are based on piezoelectric effect [22]. However, it is not easy to fabricate devices with active element size small enough to avoid spatial averaging without sacrificing sensitivity.

In the past century, fiber optic sensor technology is developing rapidly. The use of optical fiber in temperature [23], strain [24], pressure and acoustics [25] , refractive index [26], humidity [27] and vibration [28] measurements has been explored. Optical pressure and acoustic sensors have the following advantages over conventional sensors: (1) Immunity to electromagnetic interference, (2) High spatial resolution, (3) small size, light weight, (4) Large bandwidth [29], (5) Resistance to high temperature, chemical corrosion and hence suitable for hazardous environments.

Objectives: From the previous reviews, it is concluded that optical fiber sensor is a promising candidate for pressure/acoustic measurement in harsh environment. However, there still exist a series of unsolved issues in association with optical fiber sensors in practical implementations.

The main objective of this work is to develop novel optical fiber sensors using modern laser fabrication techniques that would resolve some of the current remaining problems in optical fiber pressure/acoustic sensors. Specifically, we will design, develop and demonstrate novel optical fiber pressure/acoustic sensors with enhanced sensitivity, survivability, immunity to environmental medium, large bandwidth and high directivity through laser based fabrication. The specific objectives of this research include:

1) Development and demonstration of a novel optical fiber inline extrinsic Fabry-Perot interferometer (EFPI) by femtosecond laser micromachining. The pressure sensitivity and high temperature survivability of the device are characterized experimentally. The small temperature cross-sensitivity and the unique characteristics of the device are demonstrated.
2) Investigation of acoustic characteristics of the EFPI sensor. The sensitivity, resonance frequency, and directional response of the sensor are studied theoretically and experimentally.
3) Development and demonstration of simultaneous temperature and pressure measurement using EFPI and intrinsic Fabry-Perot interferometer (IFPI).

1.4. ORGANIZATION OF THE DISSERTATION

The dissertation is organized into seven sections with their contents briefly described below:

Section 1 provides a general introduction of the research background and objective. A brief review of the current state-of-the-art sensing technologies is provided, from which the research objectives and the scientific/technical topics to be addressed by this dissertation are derived. And a brief description of the scope of the dissertation work is provided.

Section 2 describes the principle of diaphragm based pressure sensor. The principles of EFPI, the sensor's static and acoustic pressure response, and finite element analysis are described in details.

Section 3 describes the sensor fabrication, including the femtosecond laser system configuration, sensor fabrication procedure, and the advantages and challenges of femtosecond laser micromachining method.

Section 4 presents static pressure measurement using EFPI sensor. After the construction of the pressure testing system is introduced, the sensor's static pressure response is analyzed, including sensitivity, temperature dependence and high temperature stability.

Section 5 presents the acoustic pressure measurement using EFPI sensor. The sensor's performance in terms of sensitivity, resonant frequency and angular dependence are provided.

Section 6 presents simultaneous pressure and temperature measurement using EFPI and IFPI sensors.

Section 7 summarizes the dissertation work and identifies the future work.

2. PRINCIPLE OF DIAPHRAGM BASED PRESSURE SENSOR

This section will describe the basic principles of EFPI; sensor mechanical analysis including diaphragm deflection and frequency response; and signal demodulation schemes including interference phase trace and intensity trace methods.

2.1. PRINCIPLES OF EFPI

The schematic configuration of EFPI sensor is shown in Fig. 2.1. The low-finesse EFPI can be modeled using the following two-beam interference equation,

$$I = I_1 + I_2 + 2\sqrt{I_1 I_2}\cos(\frac{4\pi n_0 L}{\lambda} + \varphi_0) \tag{2.1}$$

where I is the intensity of the interference signal; I_1 and I_2 are the intensities of the reflected light at the two endfaces, respectively; φ_0 is the initial phase of the interference; L is the cavity length; n_0 is the refractive index of the medium filling the cavity (in most cases the medium is air); and λ is the optical wavelength in vacuum.

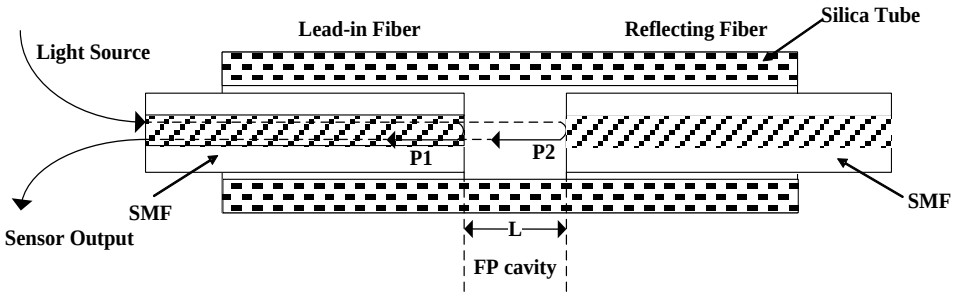

Figure 2.1 Schematic diagram of an EFPI sensor

The intensity of the interference signal reaches its minimum (P_{min}) when the phase of the cosine term in equation 1 becomes an odd number of π. That is,

$$\frac{4\pi L}{\lambda} = (2m+1)\pi \tag{2.2}$$

where m is an integer.

The two adjacent valleys at λ_1 and λ_2 in the interference spectrum have a phase difference of 2π, that is:

$$\left(\frac{4\pi}{\lambda_1}L\right)-\left(\frac{4\pi}{\lambda_2}L\right)=2\pi \tag{2.3}$$

Therefore the optical length of the cavity L can be calculated by:

$$L=\frac{\lambda_1\lambda_2}{2(\lambda_2-\lambda_1)} \tag{2.4}$$

where λ_1 and λ_2 are the center wavelength of specific interference valleys.

When the amount of optical length change is small so that the phase shift is less than 2π, the phase ambiguity issue can be avoided. The relative optical length change can be calculated based on the spectral shift of the interferogram at the featured points such as the peak, valley and the center of the interference fringes, given by

$$\Delta L=\frac{\Delta\lambda}{\lambda}L \tag{2.5}$$

where λ and $\Delta\lambda$ are the wavelength and the shift of wavelength at the interference valley, respectively.

2.2. DIAPHRAGM MECHANICAL ANALYSIS

2.2.1. Diaphragm Deflection Under Pressure. Fig. 2.2 shows a circular clamp at its edges. The diaphragm will deflect under pressure P.

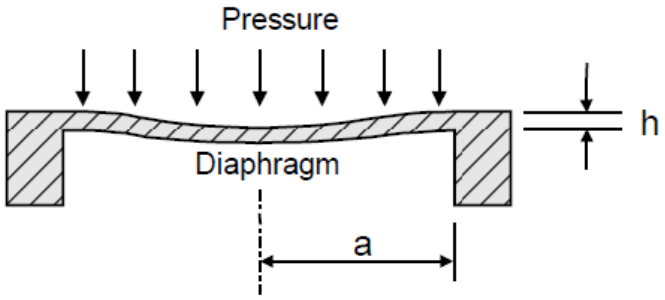

Figure 2.2 Schematic diagram of diaphragm under pressure

The ratio between the deflection and the pressure is defined as the pressure sensitivity (Y). When the input optical fiber is positioned to face the center of the diaphragm, only the center deflection Y_c is of interest, and Y_c is given by [30]

$$Y_c = \frac{3(1-\mu^2)a^4}{16Eh^3}(\mu m / psi) \tag{2.6}$$

where a and h are the diaphragm radius and thickness (in μm), respectively. E and μ are Young's modulus and Poisson's ratio of the diaphragm material.

If the diaphragm is fused silica, E = 73 GPa, μ = 0.17. Eq. (2.6) can be written as

$$Y_c = 1.71\times10^{-8}\frac{a^4}{h^3}(\mu m / psi) \tag{2.7}$$

The equations discussed above are valid only in linear region of diaphragm deflection, when the deflection is no more than 30% of the thickness of the diaphragm, which means $Y_{c,max} < 0.3h$. Therefore, the maximum pressure limit can be derived as

$$P_{max} = 1.754\times10^{8}\frac{h^4}{a^4}\,psi \tag{2.8}$$

From Eq. (2.7) and (2.8), we can conclude the diaphragm sensitivity and maximum pressure limit are related to the diaphragm thickness and radius. By increasing

the diaphragm radius, and decreasing the diaphragm thickness, the sensitivity will be increased. Conversely, increasing the thickness and decreasing the radius will increase the pressure limit.

2.2.2. Diaphragm Frequency Response. M. D. Giovanni gave the expression for the lowest natural frequency of a round diaphragm clamped at the edge as [30]

$$f = \frac{1}{\sqrt{1+\beta}} \frac{\alpha h}{2\pi a^2} \sqrt{\frac{E}{12\omega(1-\mu^2)}} \tag{2.8}$$

$$\beta = 0.669 \frac{\omega_1 a}{\omega h} \tag{2.9}$$

where α is a constant defined by the vibration mode. For the fundamental vibration mode, α=10.21. a is the diaphragm radius, h is the diaphragm thickness, E and μ are Young's modulus and Poisson's ratio of diaphragm material. ω is the specific weight of diaphragm material, and ω_1 is the specific weight of fluid surrounding the sensor.

When the diaphragm is used to measure liquid pressure, the natural frequency is reduced due to the inertia of the liquid. If the diaphragm is used in a gas, there will not be any appreciable deterioration of frequency response. In fact, in a condition where a volume of gas is trapped behind the diaphragm, a slight increase in frequency is possible as the trapped gas might act as a stiffening spring.

In order to ensure the sensor operates in the linear range, where the amplitude of diaphragm deflection is proportional to acoustic wave pressure, the fundamental natural frequency of the sensor should be at least 3 times larger than the frequency of acoustic pressure [30]. However, if the sensor's fundamental nature frequency is close to the frequency of acoustic wave, the sensor would provide ultra-high sensitivity. However, since the sensor works in a non-linear region, it is difficult to get the acoustic pressure value from the diaphragm deflection [31].

In the case of harmonic acoustic pressure, we analyze the diaphragm's response to harmonic force as below.

A mechanical system is said to undergo forced vibration when external energy is supplied to the system during vibration. For 1 degree of freedom (DOF) system under harmonic excitation, the harmonic forcing function can be expressed in complex form as $F(t) = F_0 e^{i\omega t}$, the governing equation is of the form [32]

$$m\ddot{x} + c\dot{x} + kx = F_0 e^{i\omega t} \tag{2.10}$$

The solution of eq. (1) can be written as

$$x_p(t) = \frac{F_0}{\left[\left(k - m\omega^2\right)^2 + c^2\omega^2\right]^{1/2}} e^{i(\omega t - \phi)} \tag{2.11}$$

For an undamped system, c=0, Eq. (2.11) becomes

$$x_p(t) = \frac{F_0}{k - m\omega^2} e^{i(\omega t - \phi)} \tag{2.12}$$

From above equations, the response of the system is expected to have vibration frequency the same as input force frequency. Therefore, it the diaphragm is subject to harmonic acoustic pressure, its response will have the same frequency as the frequency of acoustic pressure.

2.2.3. Angular Dependence. The amplitude response of an ultrasonic hydrophone is dependent on the angle at which the acoustic wave incidents. Three physical models with which the angular dependence of a hydrophone can be compared are (1) the circular piston in a rigid planar baffle; (2) the circular piston in a soft baffle; and (3) the unbaffled piston [33]. In a rigid baffle piston, the only part able to vibrate is the piston surface. It means the normal velocity must go to zero at the boundary. In a soft baffled piston, the acoustic potential must go to zero at the boundary, which means the pressure is zero outside the transducer surface. In unbaffled piston, the field is continuous across the boundary surface.

The expressions of far field acoustic pressure for the three models are as follows [34],

Rigid baffle piston model:

$$R = \frac{2J_1(ka\sin\theta)}{ka\sin\theta} \tag{2.13}$$

Soft baffle piston model:

$$R = \frac{2J_1(ka\sin\theta)}{ka\sin\theta}\cos\theta \tag{2.14}$$

Unbaffled piston model:

$$R = \frac{2J_1(ka\sin\theta)}{ka\sin\theta}\left(\frac{1+\cos\theta}{2}\right) \tag{2.15}$$

where J_1 is the first order Bessel function, k is wavenumber, θ is incident angle, and a is the piston radius.

Research has been conducted to study the angular dependence of fiber optic hydrophones. In 2000, J. F. Krucker *et al.* studied rigid piston approximation for computing the transfer function and angular response of a fiber optic hydrophone [35]. The rigid piston approximation is valid only for point sources on the fiber end that lies at least one wavelength inside the fiber boundary. This implies wavelength of less than 62.5 μm, i.e., acoustic frequency of more than 20 MHz. For very low frequencies, the acoustic

field distribution can be more accurately described by the unbaffled piston model. In the intermediate frequency range, the result is expected to lie between the rigid baffled piston and unbaffled piston model.

Fiber acoustic sensors are being developed for partial discharge detection and location [36]. The partial discharges can be detected acoustically and located by the triangulation method with the sensors placed inside the transformer tank. The sensor should be able to respond to acoustic waves at a large range of incident angles in order to monitor the entire transformers. In 1997, Z. Q. Zhao *et al.* investigated the directional sensitivity of an optical fiber coil based MZI sensor to acoustic signals in transformer oil [37]. For a typical partial discharge where a spectrum of acoustic emission ranging at least from 50 to 300 kHz, a fairly flat response is likely to be obtained with respect to the inclination of source to coil. In 2006, L. Song *et al.* investigated angular dependence of the frequency response of an EFPI fiber acoustic sensor for partial discharge detection [38]. A 45° monitoring range was found to exhibit an amplitude frequency fluctuation of 2.6 dB for the tested sensor.

Although an omni-directional fiber acoustic sensor is desirable in the above cases, in some applications such as photoacoustic imaging, a highly directive acoustic sensor is needed.

The directivity of an acoustic sensor depends on a number of factors, including acoustic frequency, sensor's active element radius, geometric structure, material and assembly method, etc. It is possible to design an omni-directional or directive acoustic sensor by changing these factors.

2.3. CORRUGATED DIAPHRAGM

For a plane diaphragm, the sensitivity and resonance frequency are opposing each other, according to Eq. (2.6) and (2.8). In many applications, both high sensitivity and large bandwidth are preferred. By using sensor with corrugated diaphragm, it may be possible to achieve a balance between sensitivity and bandwidth.

A corrugated diaphragm is normally made by forming concentric beads or corrugations on the diaphragm. Different MEMS techniques have been studied to fabricate corrugated diaphragms, for example, Scheeper *et al.* used the reactive ion

etching (RIE) technique to obtain corrugated diaphragms with circular corrugations [39]; Zou *et al.* used the silicon anisotropic etching technique to produce square diaphragm with rectangular corrugations [40]; And Wang *et al.* fabricated a single deeply corrugated diaphragm (SDCD) with LPCVD polysilicon process, which produces higher mechanical sensitivity than the conventional flat and shallow corrugated diaphragms [41].

In the next section, finite element analysis tool will be used to predict the performance of corrugated diaphragms.

2.4. FINITE ELEMENT ANALYSIS

Finite element analysis was conducted using ANSYS to simulate the diaphragm's performance such as sensitivity and resonance frequency.

2.4.1. Simulation Of Plane Diaphragm. The diaphragm geometry was plotted in Pro Engineer software and imported to ANSYS 7.0 workbench. Double layer 4-node shell element shell63 was used to model the diaphragm. The degrees of freedom (DOFs) of the nodes along the diaphragm's edge were set to zero as boundary conditions. The parameters of the model are listed in table 2.1. Fig. 2.3 shows the meshed model of a circular plane diaphragm.

Table 2.1 ANSYS simulation parameters

Material	Properties	Value
Fused silica	Young's modulus	73 GPa at 25^{o}C
	Poisson's ratio	0.17 at 25^{o}C
	Density	2.201 g/cm^{3}
	Diaphragm diameter	75 µm
	Diaphragm thickness	10 µm

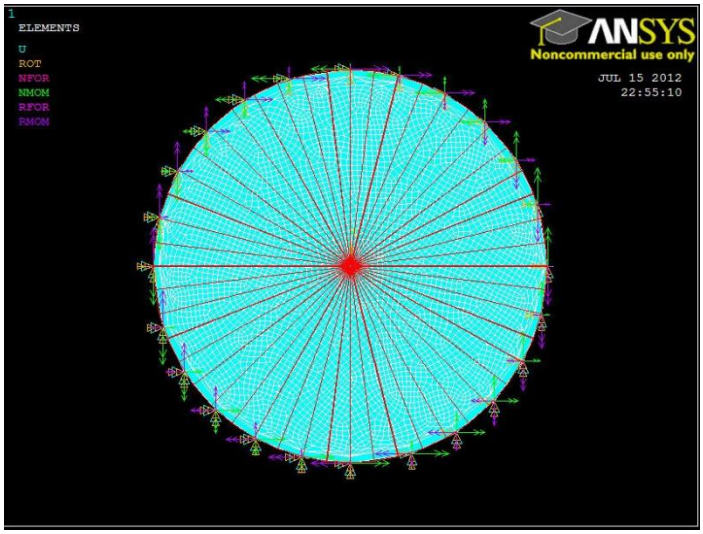

Figure 2.3 Meshed sensor diaphragm (upper surface)

Figure 2.4 is the contour plot of the deformation of the diaphragm when a mechanical pressure of 10000 Pa is applied to the surface of the diaphragm. The deflection in the center of the diaphragm is 0.48 $\times 10^{-10}$ m. From Eq. 2.7, the maximum deflection of the diaphragm in the z direction is 0.49×10^{-10} m. The results of ANSYS model show good agreement with the analytical results.

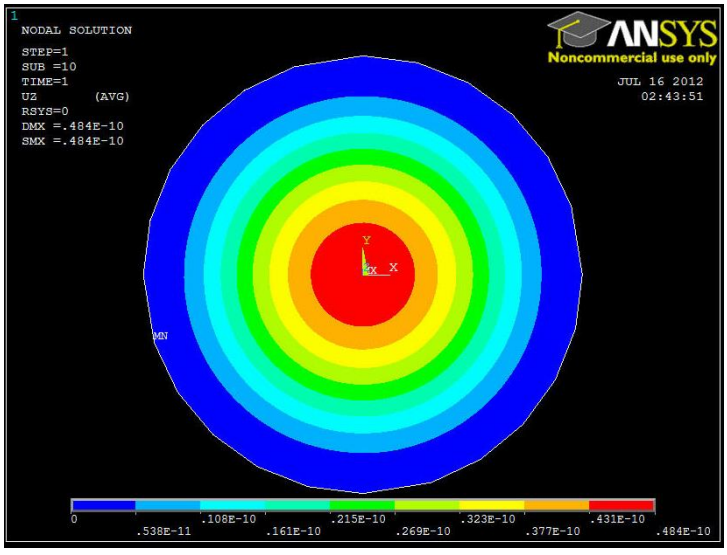

Figure 2.4 Contour plot of the deflection of the diaphragm

Fig. 2.5 shows the frequency response from 0 to 50 MHz when a sinusoidal mechanical pressure is applied to the diaphragm. The natural frequency is 20 MHz, which matches the analytical results (19.4 MHz) very well.

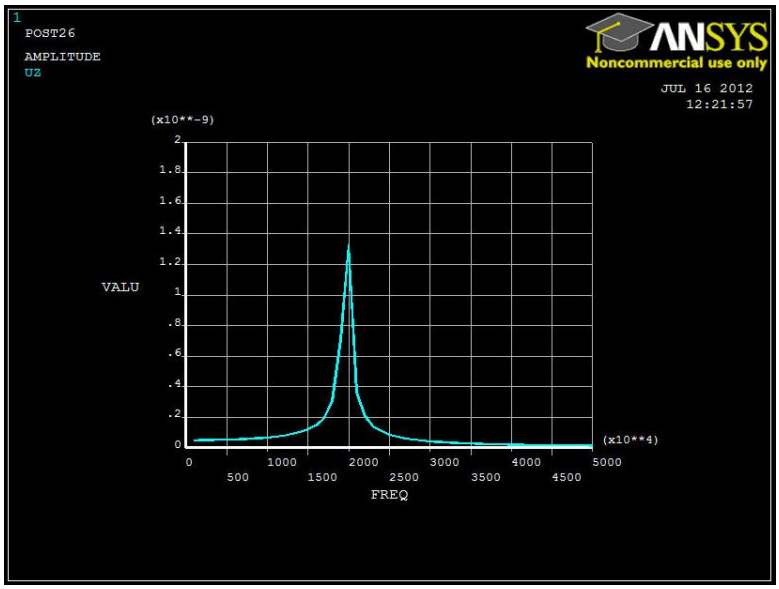

Figure 2.5 Frequency response of the diaphragm

Harmonic analysis was performed at 5 MHz, under a sinusoidal acoustic wave of 10000 Pa. The acoustic wave is launched at 0 to 90 degrees to the surface of the diaphragm, at a step of 10 degrees. The testing frequency is the center frequency of ultrasound transducer which will be used, and it is within the frequency range of medical diagnostic ultrasound systems. Figure 2.6 shows the angular dependence of the frequency response from ANSYS simulation result. The 3dB range is approximately 60 degrees.

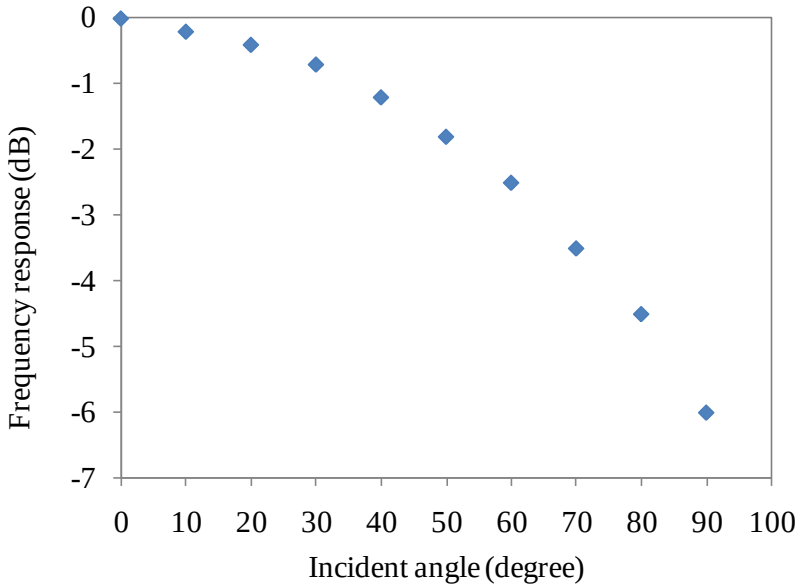

Figure 2.6 Angular dependence of the sensor at 5 MHz

2.4.2. Simulation Of Corrugated Diaphragm. For a conventional flat diaghragm, there exists an analytical expression for the mechanical sensitivity and resonance frequency. However, it becomes necessary to use the finite-element model for the simulation of the corrugated structure, because there is no analytical expression for the sensitivity and resonance frequency.

Fig. 2.7 shows the geometrical models of several corrugated diaphragms. All of them have the same volume, but their geometric structures are different. Both static and harmonic analyses have been applied to analyze their performance in terms of sensitivity and resonance frequency.

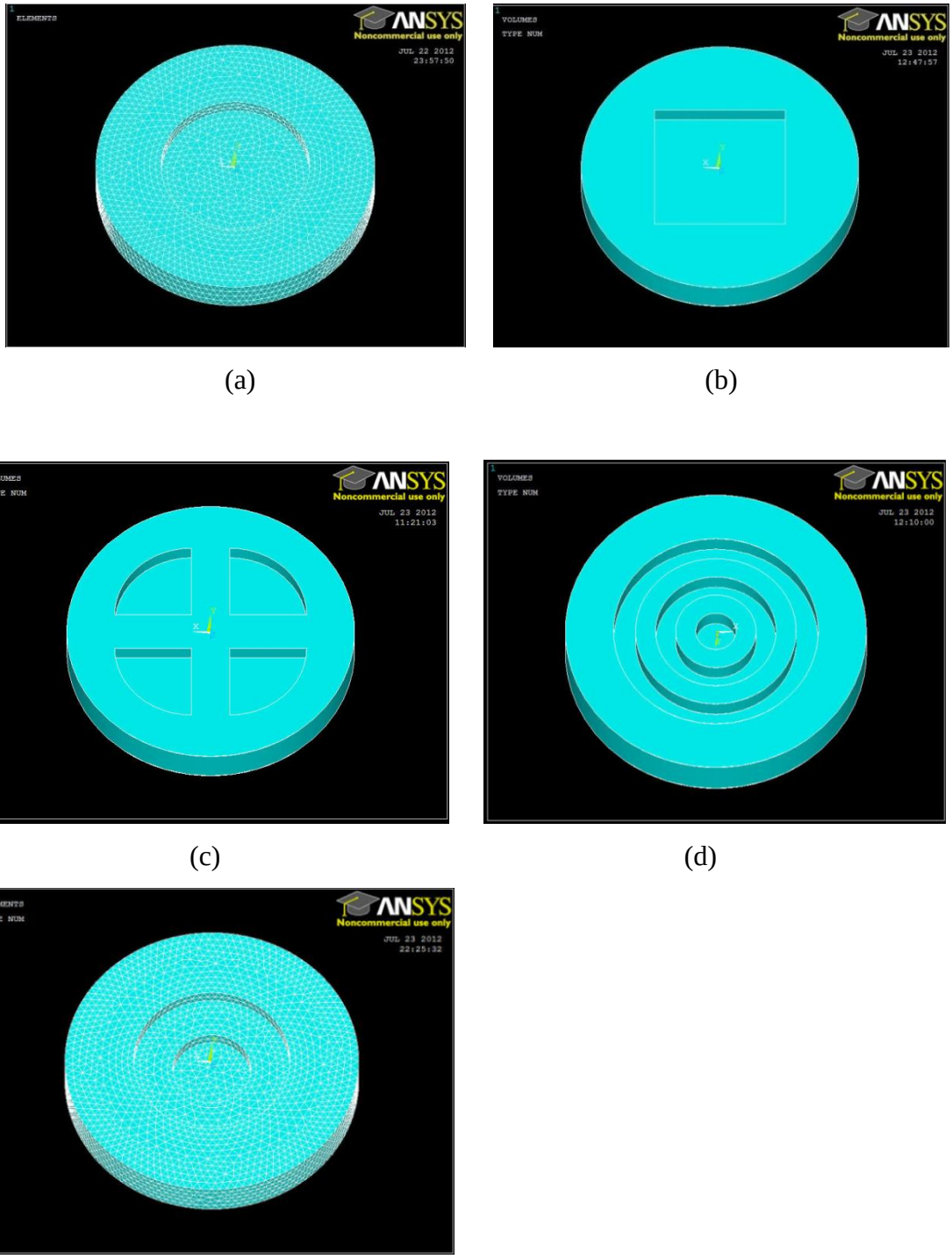

Figure 2.7 Geometric models of corrugated diaphragms

Table 2.2 lists the simulation results of the diaphragms in Fig. 2.6.

Table 2.2 ANSYS simulation results

No.	Center deflection (m)	Natural frequency (MHz)
a	0.223e-7	11.40
b	0.232e-7	11.08
c	0.178e-7	10.90
d	0.188e-7	10.63
e	0.238e-7	11.78

From the simulation results, in case (e), the diaphragm has highest sensitivity and resonance frequency. This result is the same as expected, because the diaphragm has maximum deflection at the center.

2.5. SIGNAL PROCESSING

The intensity of EFPI interference signal is a periodic function of the cavity length, the refractive index and the wavelength. For most sensing applications, the interference signal needs to be processed to obtain either the absolute value or the relative change of the cavity length (or the refractive index) that is related to the physical (or chemical) environment of interest. Although many signal processing methods have been studied in the past, the white light interferometry method produces the highest accuracy. White light interferometry commonly uses a broadband source to excite the interferometer and an optical spectrum analyzer (OSA) to record the interference signal in the spectral domain.

2.5.1. Period Tracking Method. According to Eq. (2.1), the two adjacent interference minimums have a phase difference of 2π. That is

$$\left(4\pi Ln/\lambda_{v1}+\varphi_0\right)-\left(4\pi Ln/\lambda_{v2}+\varphi_0\right)=2\pi \tag{2.16}$$

where λ_{v1} and λ_{v2} are the wavelengths of two adjacent valleys in the interference spectrum. The optical length of the FP cavity, defined as the product of the cavity length and the refractive index, can thus be found as

$$L \cdot n = \frac{1}{2} \frac{\lambda_{v1} \lambda_{v2}}{\lambda_{v2} - \lambda_{v1}} \tag{2.17}$$

In theory, Eq. 2.17 can be used to calculate either the absolute refractive index (n) or the absolute length L of the cavity if one of them is known. However, the measurement based on Eq. 2.17 has a poor resolution because the period is not a sensitive function of the optical path change.

The minimum detectable change in optical length of FP cavity (S_l) is defined as the standard deviation of the measurement uncertainty of the optical length of FP cavity. When λ_{v1} and λ_{v2} are assumed to be two independent random variables, S_l can be derived from Eq. (2.17) and expressed into:

$$\begin{aligned} S_l &= \sqrt{(\frac{\partial l}{\partial \lambda_{v1}})^2 (S_{\lambda_{v1}})^2 + (\frac{\partial l}{\partial \lambda_{v2}})^2 (S_{\lambda_{v2}})^2} \\ &= \sqrt{\frac{{\lambda_{v1}}^4}{4(\lambda_{v2} - \lambda_{v1})^4} (S_{\lambda_{v1}})^2 + \frac{{\lambda_{v2}}^4}{4(\lambda_{v2} - \lambda_{v1})^4} (S_{\lambda_{v2}})^2} \end{aligned} \tag{2.18}$$

in which $S_{\lambda 1}$ and $S_{\lambda 2}$ represent the standard deviations of the wavelength measurement of the two consecutive valleys, respectively. Determined from the performance specifications of a particular OSA instrument, $S_{\lambda 1}$ and $S_{\lambda 2}$ are equal or $S_{\lambda 1} = S_{\lambda 2} = S_{\lambda}$ since the instrument has consistent measurement accuracy of wavelength within the specified observation bandwidth. In addition, within a relatively small observation spectrum range, both λ_1 and λ_2 can be approximated by the center wavelength of the range, λ_0. As a result, Eq. (2.18) can be simplified into:

$$S_l \approx S_\lambda \frac{{\lambda_0}^2}{\sqrt{2}(\Delta\lambda)^2} \tag{2.19}$$

where $\Delta\lambda$ is the wavelength difference between the two consecutive valleys. For the estimation of measurement errors, $\Delta\lambda$ at a given cavity length can be considered as a constant within the wavelength bandwidth of observation though $\Delta\lambda$ increases with wavelength. In this case, Eq. (2.19) indicates that the minimum detectable cavity length increases quadratically with cavity length as $\Delta\lambda$ decreases.

2.5.2. Phase Tracking Method. In many cases, only the relative refractive index change is of interest and the range of refractive index variation is small so the phase shift is less than 2π. In this case, the phase ambiguity issue can be avoided. The relative refractive index change can be calculated based on the spectral shift of the interferogram.

The interference signal reaches its minimum (I_{min}) when the phase of the cosine term becomes an odd number of π. That is $I = I_{\min}$, when

$$4\pi n \cdot L / \lambda_v + \phi_0 = (2m+1)\pi \tag{2.20}$$

where m is an integer and λ_v is the center wavelength of the specific interference valley. In Eq. (2.20), taking the derivative of n with respect to λ_v, one finds:

$$dn / d\lambda_v = [(2m+1)\pi - \phi_0] / 4\pi L \tag{2.21}$$

Assuming the cavity length L is maintained constant during measurement, Eq. (2.21) indicates that the refractive index is a linear function of the valley wavelength, or the sensitivity of the FPI sensor is a constant. The amount of refractive index change (Δn) can thus be computed based on the wavelength shift of a particular interference valley using the following equation,

$$\Delta n = n \cdot \Delta\lambda_v / \lambda_v \tag{2.22}$$

where the relative refractive index change is directly proportional to the spectral shift of the interferogram. It is worth noting that Eq. (2.22) is also applicable to other characteristic spectral positions such as the interference peak and the center point of the interferogam. The advantage of using the center point in calculation is that its spectral position can be resolved with a higher resolution compared to the valley or the peak that typically has a flat bottom or top. In addition, curve fitting of the interference fringe can also improve the measurement accuracy. Since the minimum $\Delta\lambda_v$ can be represented by the instrument measurement accuracy or S_λ, the resolution of the phase tracking method decreases linearly with the cavity length.

Comparing Eq. (2.19) and Eq. (2.22), one finds that Eq. (2.19) can be used to calculate the absolute FP cavity optical length while Eq. (2.22) only provides the relative change of the FP cavity optical length, or change of refractive index given a fixed physical length. However, the calculation based on Eq. (2.22) has a much higher resolution than that obtained using Eq. (2.19).

2.5.3. Interference Frequency Tracking Method. The spectral interferogram of an EFPI typically represents a harmonic function of wavenumber with a dominant frequency known as interference frequency. By taking the Fourier transform of such an interferogram, an approximate delta function of cavity length corresponding to the interference frequency is obtained. The cavity length of the EFPI, *l*, can be calculated by:

$$l = \frac{n\pi}{\left(v_E - v_S\right)} \tag{2.23}$$

in which v_S and v_E are the wavenumbers of the starting and ending points of an observation bandwidth, respectively, and *n* is an integer representing the Fourier series index.

It can be easily observed from Eq. (2.23) that the minimum detectable cavity optical length change using spatial Fourier transform method is $\pi/(v_E - v_S)$ when n=1. For

a light source with a spectrum width of 100 nm, the detectable cavity length change is approximately 12 μm. Given that the physical cavity length of an optical fiber inline FPI is 60 μm, optical length higher than 20% is able to be detected using this signal processing method. The measurement resolution then requires a broader bandwidth of the optical source, which can only be provided by limited equipment available in the market.

In this study, phase tracking method will be used, because the phase shift is less than 2π, using phase tracking method will provide higher resolution than the other methods.

3. SENSOR FABRICATION

3.1. CURRENT FABRICATION METHODS

Several methods have been reported to fabricate thin diaphragm based FP pressure sensor. In terms of sensor fabrication, FP pressure sensors can be categorized into the following categories: 1) pressure sensors fabricated by using conventional machining and assembly techniques such as anodic bonding [42] , 2) all-silica pressure sensors fabricated by using splicing, fusion bonding, cleaving, and wet etching of optical fibers and silica tubes [25, 43], 3) pressure sensors fabricated by using clean-room micro fabrication techniques such as photo lithography, etching, and bonding and 4) pressure sensors with a polymer diaphragm attached to the end of a hollow core tube [44, 45].

3.2. INTRODUCTION TO FEMTOSECOND LASER MICROMACHINING

A femtosecond laser is a laser which emits optical pulses with a duration well below 1 ps, i.e., in the domain of femtoseconds (1 fs = 10^{-15} s). It thus also belongs to the category of ultrafast lasers or ultrashort pulse lasers. The generation of such short pulses is nearly always achieved with the technique of passive mode locking.

The development in fs laser micromachining technology has enabled fabrication of micro-devices that are difficult to make using other methods. Direct exposure of most solid materials (including fused silica glass) to high power fs laser pulses may lead to the ablation of a thin layer of materials at the laser focal point. Due to the multi-photon nature of the laser-material interaction, the ablation process can be conducted on the material surface as well as within its bulk. As a result, three-dimensional (3D) micro photonic devices can be fabricated with sub-micron accuracy. Examples of optical devices include optical waveguide[46, 47], microlens and microlens arrays[48, 49], fiber Bragg gratings[50, 51], fiber inline FPI [52, 53] and MI [54]. Our group has reported several novel fiber optic devices in recent years. For example, T. Wei *et al.* demonstrated an inline FPI device with a fringe visibility of 16 dB by fs laser one-step micromachining a micro-notch on a single-mode fiber [52]. L. Yuan *et al.* demonstrated a fiber inline Michelson interferometer fabricated by micromachining a step structure at the tip of a single-mode optical fiber using a fs laser [54]. The step structure splits the fiber core into

two reflection paths and produces an interference signal. A fringe visibility of 18 dB was achieved. Temperature sensing up to 1000°C was demonstrated using the fabricated assembly-free device.

In this study, we used a high repetition rate Ti: Sapphire laser (Coherent RegA 9000). It has the following features [55]:

- CW-pumped regenerative amplifier
- High repetition rate, variable up to 250 kHz
- Ultra stable operation
- Near-diffraction-limited output beam
- Integrated pulse compressor Multiple OPA pumping
- Advanced electronic control
- 2-box solution with Vitesse Duo

The high repetition rate (250 kHz, 4 uJ per pulse) fs laser pulse is suitable to fabricate thin diaphragm as it allows us to fine-tune the laser power precisely around the damage threshold so that crack propagation can be avoided to improve mechanical strengths.

3.3. EFPI SENSOR FABRICATION PROCEDURE

To fabricate the EFPI sensor, a micro hole was first drilled into the cleaved endface of a single mode fiber (SMF) by fs laser micromachining. The inner surface of the laser-drilled micro hole had quasi-distributed structures of submicron sizes and a low optical reflectivity. The hole-drilled SMF was then spliced to another SMF to form a sealed air cavity in between two fibers. We adjusted the fusion splicer settings to avoid the collapsing of the hole. We used Sumitomo Type-36 Fusion Splicer, manual mode with the following settings: Arc duration 0.6, prefusion 0.1, arc gap 5, overlap 10, arc power 7. With this setting, the collapsing of the hole has been avoided. During fusion splice, the rough structure of the micro hole surface was melted by the arc. As a result, the surface became smooth and the reflectivity increased. Precision fiber cleaving was applied to cut the fiber so that a thin piece of fiber was left to perform as the diaphragm. Finally the as-cleaved diaphragm was thinned and roughened by fs laser. During fs laser micromachining, the sensor was mounted on a computer controlled high-precision 3D

stage with a resolution of 0.1 μm. Light pulses generated by a regeneratively amplified Ti: Sapphire laser (Coherent RegA 9000, 200 fs pulse duration, 250 kHz repetition rate and 800 nm central wavelength) were focused onto the fiber endface or diaphragm surface through a microscope objective (20× magnification, 0.4 numerical aperture).

The laser power could be changed by adjusting the laser beam optics, including a half-wave plate, a polarizer and several neutral density filters. The actual laser energy used for fabrication was approximately 0.4 mJ per pulse. The diameter and depth of the hole could be varied flexibly. The diaphragm thinning process was also performed layer-by-layer with a step size of 0.5 μm. The fabrication was completed when preset depth scan was reached. Fig. 3.1 and Fig. 3.2 show the experimental setup of the fabrication system. Fig. 3.3 (a) shows an fs laser drilled hole with diameter of ~ 80 μm and thickness of ~10 μm. We can see from the figure the wall of the hole has some degree of slope. This is due to the accumulation of fiber debris around the corners of the hole in laser fabrication. Fig. 3.3 (b) shows SEM image of a diaphragm with a small rectangular hole cut at its center using focused ion beam. The thickness of this diaphragm is estimated from the length bar to be ~ 4 μm. The micro structure on the diaphragm surface is clearly visible. In Fig. 3.3 (c), half of the sensor head was cut out using fs laser to expose the sealed hole and the diaphragm. This particular sensor had a cavity with the diameter of 70 μm and the length of 100 μm [56].

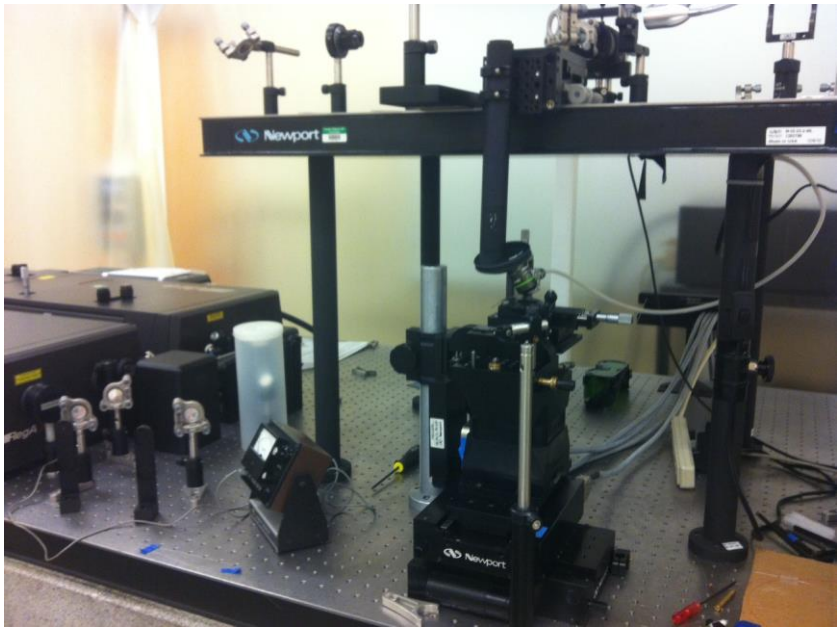

Figure 3.1 Photo of femtosecond laser micromachining system

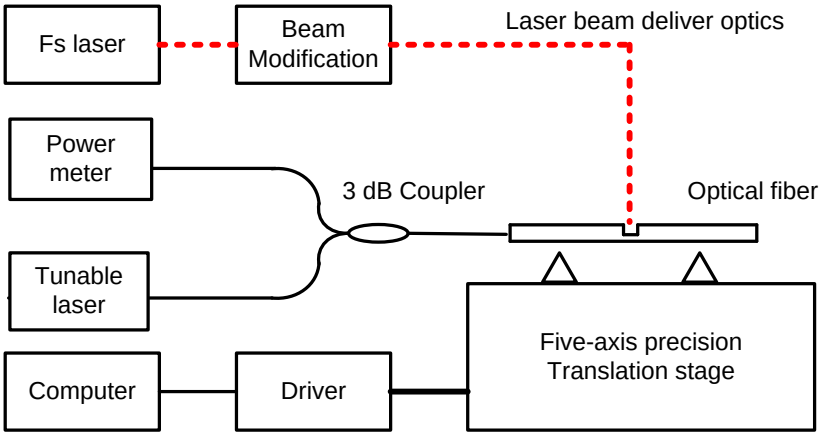

Figure 3.2 Fiber inline FPI device fabrications using fs laser [57]

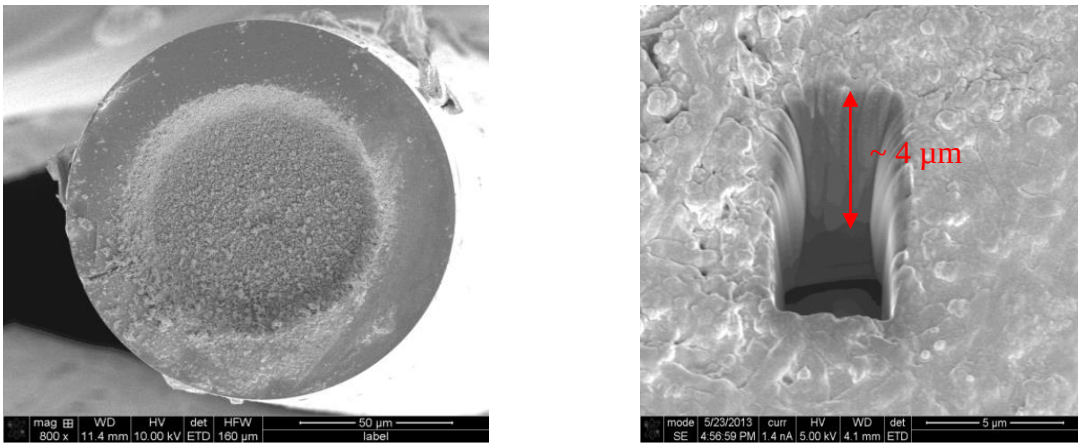

(a) (b)

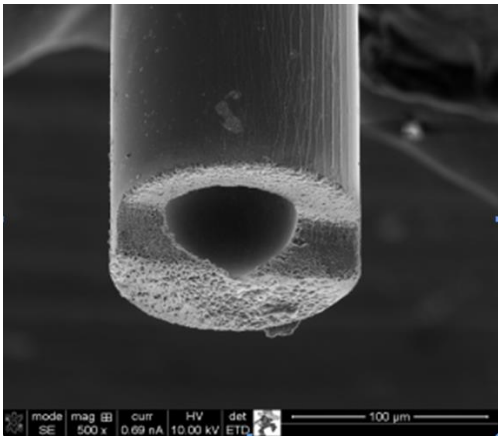

(c)

Figure 3.3 SEM images of femtosecond laser micromachined EFPI (a) laser drilled micro hole (b) lateral cut view of the diaphragm (c) cut out view of the sensor head

A number of sensors were fabricated. The interference spectra of the fabricated sensors were acquired using a system shown in Fig. 3.4. The system consisted of a broadband light source (Agilent 83437A), a fiber circulator (Thorlabs SM fiber optic circulator 6015-3) and an optical spectrum analyzer (OSA, Ando AQ6319). The optical transmission and reflection insertion losses of the circulator have been calibrated in the wavelength range of 1300 – 1700 nm.

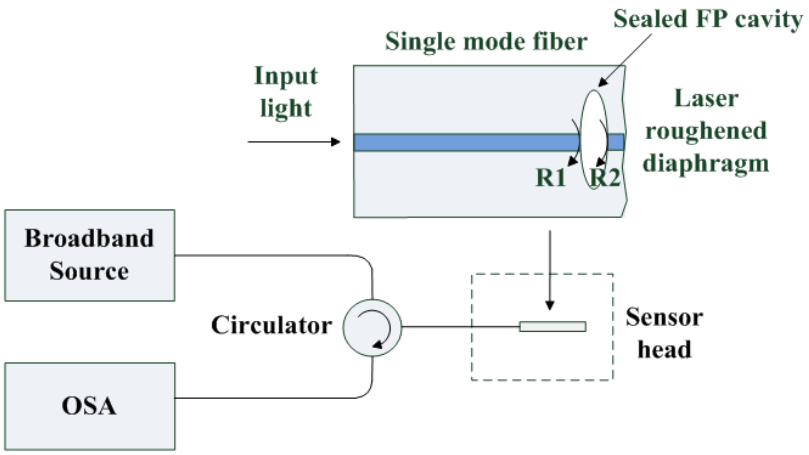

Figure 3.4 Schematic of the sensor interrogation system

Fig. 3.5 (a) and (b) plot the interference fringes of a typical sensor before and after fs laser ablation in air and in water. The sensor had a cavity length of about 8 μm and a hole diameter of 75 μm. The cavity length was calculated to be 7.97 μm based on the interference fringes using the method reported in reference [58]. The as-cleaved diaphragm had a thickness of about 25 μm, measured by an optical measuring microscope (Nikon Measurescope UM-2). As shown in Fig. 3.5(a), before laser ablation the sensor had a distorted spectrum, resulting from the superposition of three-beam interferences. In addition, when the surrounding medium changed from air to water, the fringes changed significantly, suggesting that the as-cleaved diaphragm would introduce measurement errors when the surrounding medium changes. The laser roughened diaphragm significantly reduced the reflection from the outer surface. Immersion of the sensor head into water did not incur any noticeable change to the interferogram, suggesting the immunity of the sensor to variations in surrounding media.

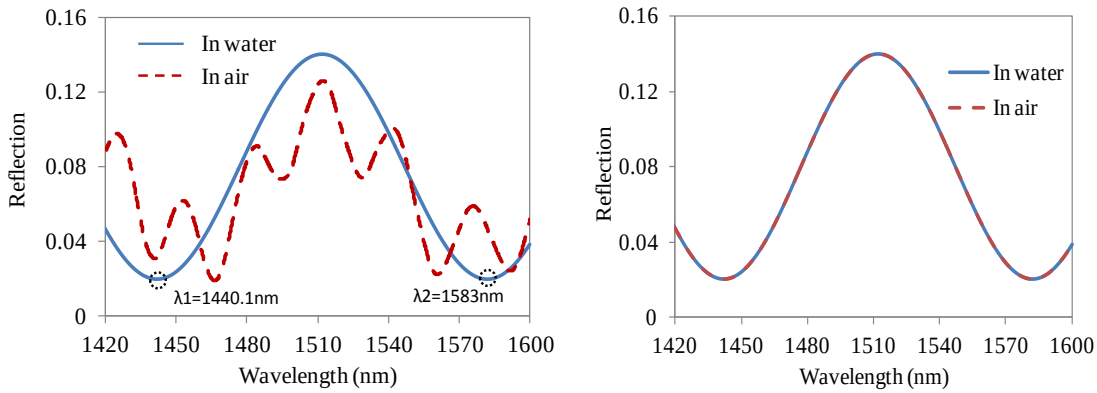

Figure 3.5 Typical interference spectra of the fiber FPI sensor in air and water. (a) Before laser ablation of the diaphragm, (b) After laser ablation of the diaphragm.

3.4. IFPI SENSOR FABRICATION

The IFPI sensor was fabricated using the same fs laser. In fabrication, a single mode fiber was clamped at two ends by fiber clamps and placed in a water filled glass box. The glass box was further fixed to a three-axis precision stage. A water immersion lens (Olympus UMPlanFL 20X) was used to focus the fs laser into the fiber core. The IFPI can be made by either inscribe two points or two parallel lines in the fiber core, as shown in Fig. 3.6. The fabrication procedure is as follows. First, the position of fiber was adjusted with the help of CCD camera to focus the fs laser into the fiber core. Due to the difference of light focal length in air and water, the fiber was moved by an offset distance in the vertical direction to compensate for the difference. After the first reflector was created, the fiber was moved by the targeted cavity length, and then the second reflector was created. An OSA was used to monitor the interference spectrum in-situ.

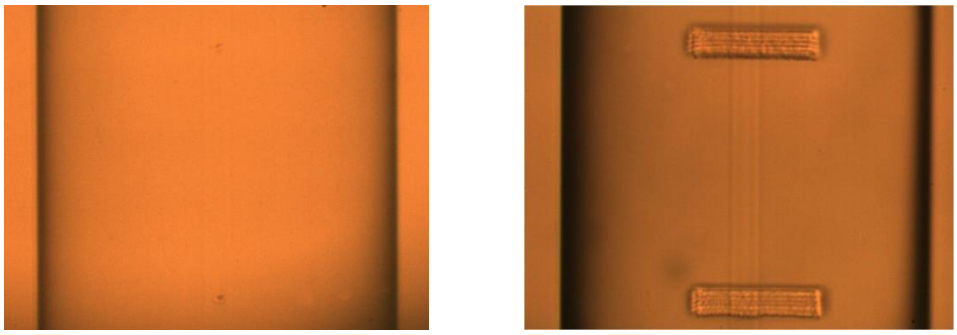

(a) (b)

Figure 3.6 Microscopic images of IFPI sensor (a) Two points IFPI (b) Two lines IFPI

Fig. 3.7 shows a typical interference spectrum of IFPI fabricated by fs laser. The loss is ~30 dB, so the reflectivity of the laser ablated point is ~0.1%. The interference fringe contrast is ~20 dB.

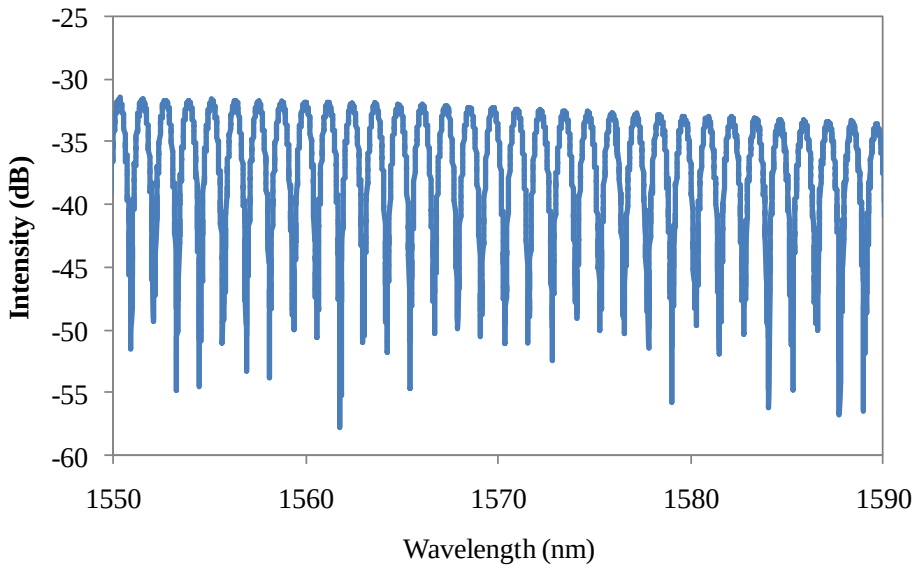

Figure 3.7 Interference spectrum of IFPI

3.5. ADVANTAGES AND CHALLENGES

3.5.1. Advantages. There are quite a few advantages of using fs laser to fabricate micro sensors. First, it is possible to fabricate 3-D microstructures of desirable shape with sub micrometer precision using fs laser. Second, the focal point of the fs laser is

adjustable to fabricate on both the cladding and core of the fiber. The flexibility of laser focal point enables fabrication of many fiber inline devices, such as FBG, LPFG, IFPI, fiber inline polarizer, etc. Third, fs laser fabrication creates a rough surface with nanostructures, which could be utilized for specific purposes. X. Lan *et al.* reported a surface-enhanced Raman-scattering fiber probe fabricated by fs laser [59]. Direct fs laser ablations resulted in nanostructures on the cleaved endface of a multimode optical fiber. The laser-ablated fiber endface helps to generate high-quality SERS signal. And as discussed in this section, the rough surface in fs-laser fabricated pressure sensor helps to eliminate reflections at the diaphragm endface. This not only facilitates signal processing, but also makes the sensor immune to refractive index change in the surrounding medium. Fourth, the all-silica structure avoids the problem of CTE mismatch and is good for applications in high temperature. Finally, the fabrication procedure does not involve any hazardous chemicals, like HF in chemical etching.

3.5.2. Challenges. Some challenges still exist in fs laser micromachining. First, it is difficult to fabricate a deep structure with its wall perpendicular to the fiber axis due to the cone shape of the laser beam, and debris of fiber accumulating at the wall of the hole. The deepest hole that we have drilled with acceptable bottom flatness was about 20 μm. When the hole depth creases, the shape will become like Fig. 3.8.

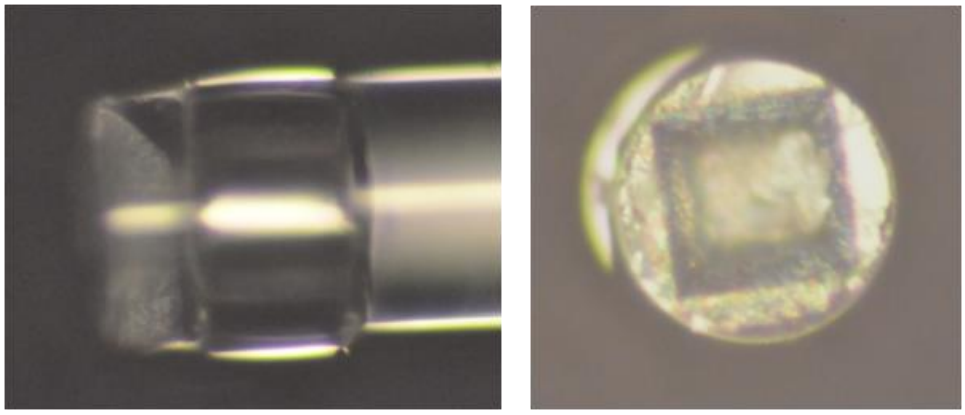

(a) (b)

Figure 3.8 Microscopic images of cone shape hole (a) lateral view (b) top view

Next, currently it is difficult to fabricate diaphragm thinner than 2 μm as the ultra-thin diaphragm tends to break during fabrication. Possible reasons include the non-ideal focal length of the fs laser, and the degradation of mechanical strength of fs laser ablated surface.

Additionally, the performance of fs laser is subject to many environmental conditions, i.e., temperature, humidity, dust, etc. Special attention needs to be paid to keep the laser room in controlled environmental conditions.

4. STATIC PRESSURE TEST

4.1. PRESSURE SENSITIVITY CALIBRATION

The pressure sensitivities of fabricated sensors were characterized. The sensor was sealed in a pressure chamber where the air pressure was supplied using a compressed Argon gas cylinder and controlled by a pressure controller (MKS640). The pressure controller could supply a static pressure up to 6.895×10^5 Pa and the precision of the pressure output was 0.5% of the full scale according to the specification.

Fig. 4.1 shows the measurement results obtained from one sensor, where the changes in cavity length are plotted as a function of the applied pressure. Within the pressure range of 6.895×10^5 Pa, the center of the diaphragm deflected linearly as the pressure changed. Based on the linear fitting curve, the sensitivity of the sensor was calculated to be 2.8×10^{-4} nm/Pa. To test the sensor's repeatability, measurements were performed four times at each pressure level. The largest difference among the four time measurements was 0.3%.

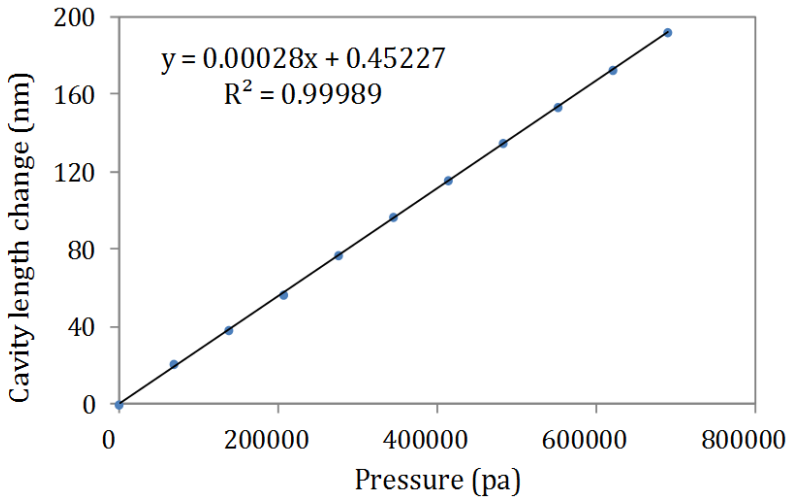

Figure 4.1 Pressure induced inteferogram shift of EFPI sensor

The diaphragm thickness could be calculated from measured sensitivity. The calculated diaphragm thickness was 2.6 μm, which was close to the target value after

laser thinning. Given a wavelength measurement resolution of 0.05 nm of the OSA, the resolution of the pressure sensor was estimated to 180 Pa.

4.2. HIGH TEMPERATURE TEST

A potential application of the developed sensor is in situ pressure monitoring in a high temperature environment. Minimizing the temperature dependence of the sensor becomes an important issue. To measure the temperature sensitivity, the sensor was placed in an electrical tubular furnace and heated from room temperature (20 °C) to 700 °C, and cooled down to 20 °C again. Measurements were performed both in temperature increase and decrease cycles. The largest difference between measurement results in the two cycles was 1%. Fig. 4.2 plots the wavelength shift of the interferogram as a function of the ambient temperature. The sensor successfully survived at 700 °C and exhibited a linear response to temperature variation. The sensor had a temperature sensitivity of 4.44 $\times 10^{-3}$ nm/°C based on the linear fitting curve in Fig 4.2. The air gap change was mainly induced by thermal expansion of the cavity, which was hosted inside fused silica fiber cladding with a coefficient of thermal expansion (CTE) of 5.5×10^{-7} /°C. Given that the sensor had a cavity length of 7.97 μm, the thermal expansion ratio was calculated to be 5.57×10^{-7} /°C, which was very close to the CTE of fused silica. The slightly larger temperature dependence of the sensor, in comparison with the CTE, could be caused be the expansion of sealed air, which pushed the thin diaphragm outwards as the temperature increased. Nevertheless, the sensor had very small temperature dependence, suggesting low temperature cross-sensitivity in pressure measurement. According to the measurement results, the temperature-pressure cross sensitivity is found to be less than 15.86 Pa/°C.

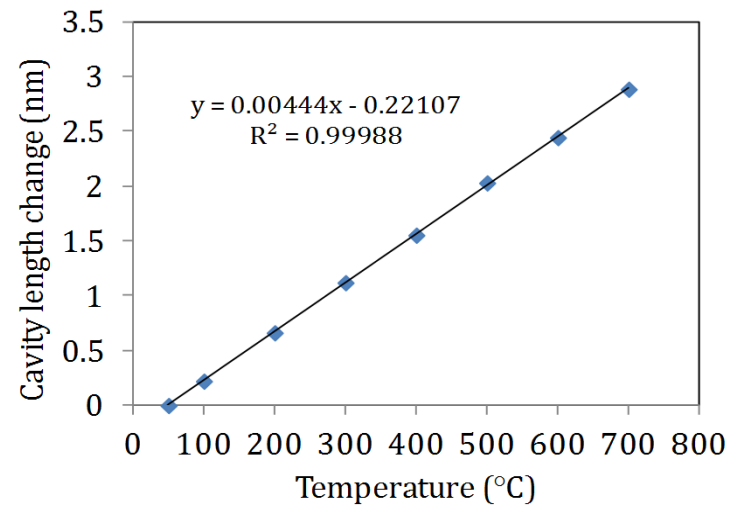

Figure 4.2 Sensor response to temperature changes

4.3. AUTOGENIC PRESSURE TEST

The sensor was tested for measurement of the autogenic pressure of water vapor at high temperatures. The autogenic pressure is the pressure exerted by a vapor in thermodynamic equilibrium with its condensed phases (solid or liquid) at a given temperature in a closed system, illustrated in Fig. 4.3.

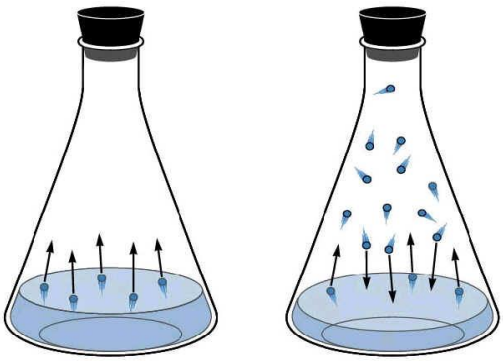

Figure 4.3 Autogenic pressure of water vapor

Fig. 4.4 shows the relationship between temperature and vapor pressure. The vapor pressure is an exponential function of the temperature.

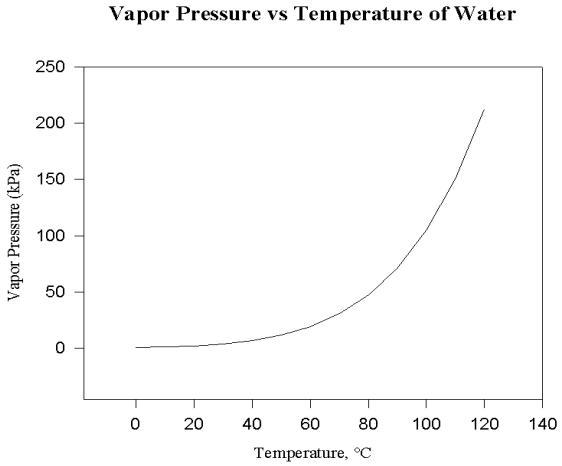

Figure 4.4 Water vapor pressure as a function of temperature

According to reference [60], the saturation water vapor pressure is

$$P = P_0 \exp\left[24.921\left(1-\frac{T_0}{T}\right)\right]\left(\frac{T_0}{T}\right)^{5.06} \tag{4.1}$$

where P is the absolute vapor pressure, T is the temperature, T_0 = 273.16 K, P_0 = 611.657 Pa.

To perform the experiment, the sensor was sealed in a stainless steel tube, with part of the tube filled with water. The tube was placed in an electric oven and heated from room temperature (20 °C) to 200 °C. Measurements were performed three times at each temperature level. The largest difference among the three time measurements was 0.5%. Fig. 4.5 plots the theoretical and measured pressures at different temperatures. The theoretical values were calculated by adding the result from Eq. (4.1) and atmospheric pressure at room temperature. The measured values were obtained by measuring the wavelength shifts of the interferogram and converting them to pressure changes using the pressure sensitivity (2.8×10^{-4} nm/Pa) obtained from pressure testing (Fig. 4.1).
The sensor successfully survived the high-temperature and high-pressure conditions. The theoretical, experimental values and their difference are also listed in the inset table. In general, the measured pressures were in good agreement with the theoretical values, but the measured values were always larger than the theoretical values. In general, the

difference became larger as temperature increased. We believe that the difference was mainly caused by the thermal expansion of the cavity, or in other words, the temperature cross-sensitivity of the device. Other error sources might include the inaccuracy of the model given in Eq. (4.1), and imprecise measurements of the initial cavity length, pressure sensitivity, and temperature readings of the oven. Nevertheless, the experiment demonstrated that the feasibility of using the sensor to measure high pressure in a high temperature environment without temperature compensation.

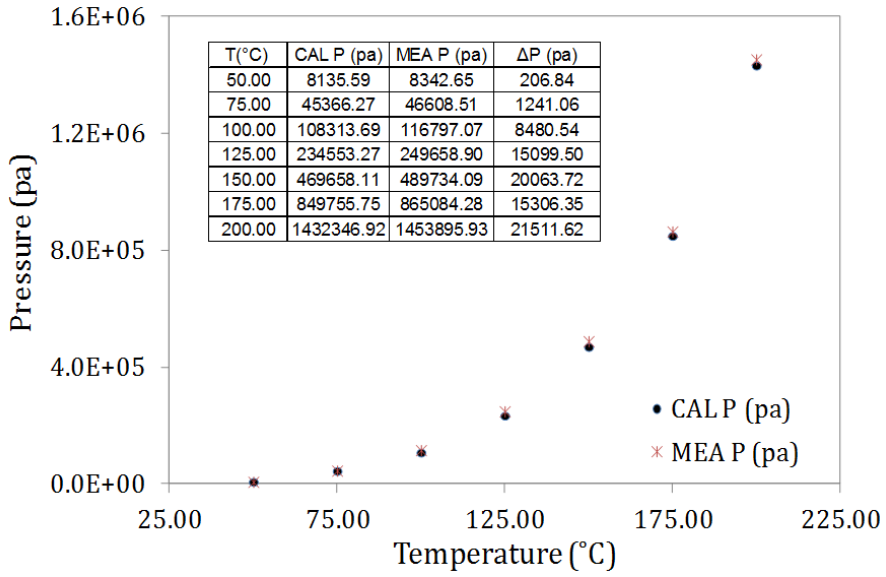

T(°C)	CAL P (pa)	MEA P (pa)	ΔP (pa)
50.00	8135.59	8342.65	206.84
75.00	45366.27	46608.51	1241.06
100.00	108313.69	116797.07	8480.54
125.00	234553.27	249658.90	15099.50
150.00	469658.11	489734.09	20063.72
175.00	849755.75	865084.28	15306.35
200.00	1432346.92	1453895.93	21511.62

Figure 4.5 Measured and calculated water vapor pressures at different temperatures. CAL P: theoretical pressure, MEA P: measured pressure, ΔP: difference of MEA P and CAL P

4.4. SUMMARY

In summary, a diaphragm-based miniature fiber optic FPI pressure sensor was fabricated by fs laser micromachining. The sensing head consists of a laser micromachined FPI air cavity and a fused silica diaphragm with its outer surface thinned and roughened by fs laser. The diaphragm thickness can be controlled to vary the sensitivity for pressure measurement. Thin diaphragms with thicknesses as small as 2.6 μm are achievable. A pressure sensitivity of 2.8×10^{-4} nm/Pa and a resolution of 180 Pa were demonstrated. The sensors have been tested at high temperatures up to 700 °C, showing a linear response to temperature with low temperature sensitivity of $5.57\times10^{-}$

^{7}/°C, corresponding to a small pressure-temperature cross sensitivity less than 15.86 Pa/˚C. The sensor has also been demonstrated for measurement of autogenic pressures of water vapor up to 200 ˚C. Without temperature compensation, the pressure measurement results agreed well with those calculated based on the theoretical model. Compared with previously reported fiber-tip pressure sensors, the sensor presented here has less temperature cross-sensitivity. It is also insensitive to variations in ambient refractive index. The diaphragm thickness and diameter can be controlled with fs laser micromachining to adjust the sensitivity and measurement range. The sensor's pressure sensitivity is relatively low compared with sensors made of other diaphragm materials such as polymer, but it has a larger pressure range and can work at higher temperature. The proposed sensor is useful for pressure measurement in a high temperature harsh environment.

5. ACOUSTIC PRESSURE TEST

5.1. SYSTEM OVERVIEW

The fiber optic acoustic pressure measurement system is the combination of two parts: the sensing element fabricated at the tip of an optical fiber, and an interrogation unit which provides illumination and signal processing for sensor readout.
The interrogation unit includes the following components: a tunable laser as the light source, a photodiode to convert the optical signal to electrical signal, a tunable amplifier to amplify the electrical signal from the photodiode, and an oscilloscope to analyze the signal.

One of the most important components in the interrogation unit is the tunable laser. The laser provides light to illuminate the sensor, which is subsequently modulated by acoustic pressure and hence enables the detection of ultrasound fields. It also allows the optimization of acoustic sensitivity through its ability to tune through a range of wavelengths. In this work, we used Agilent 8168F tunable laser, it has a tunable wavelength range of 1480-1590 nm, wavelength resolution of 0.001 nm, and output power from -7 to 7 dBm.

A fiber pigtailed photodiode or an opto-electronic converter is used to convert optical signals to electronic signals. And an amplifier may be used if the signal is weak. One requirement for the photodiode and amplifier is the bandwidth range.
A digital oscilloscope (Tektronics DPO 7254) is used to record and analyze the acoustic signals. The oscilloscope has bandwidths from 500 MHz to 3.5 GHz, up to 40 GS/s Real-Time sample rate on one channel. It has many built-in functions such as averaging, filtering, spectrum analysis, etc.

5.2. OPERATING POINT BIASING

In order to use the sensor to measure acoustic pressure, the system must first be biased to ensure optimum acoustic sensitivity. This is achieved by varying the laser wavelength and finding the wavelength that corresponds to the peak derivative of the interferometer transfer function. This process is operating point biasing and must be

carried out prior to an acoustic measurement. We used OSA to get the sensor spectrum and find the operating point.

Fig. 5.1 shows a typical interference fringe of EFPI and its operating point.

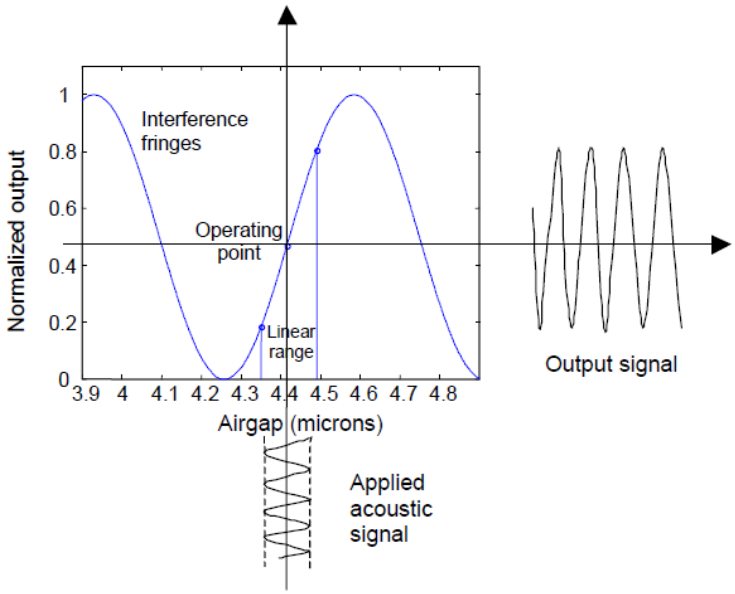

Figure 5.1 Operating point of interference fringe

5.3. ACOUSTIC SENSOR CHARACTERIZATION

Before the fiber optic acoustic sensor can be used to make quantitative measurements of acoustic fields, it must be characterized in terms of its acoustic performance. There are three main characteristics which need to be determined; the sensitivity, the frequency response and the directional response. The sensitivity determines the minimum acoustic pressure the hydrophone can detect. The frequency response determines the variation of the sensitivity with acoustic frequency. Finally, the directional response can be used to give an indication of the spatial averaging properties of the acoustic sensor. Besides, the signal-to-noise ratio, stability and linearity of the sensor are also measured. The sensor was tested in air and water environment as microphone and hydrophone.

5.3.1. Sensor Test In Air. Fig. 5.2 illustrates the experimental setup for acoustic measurement in air. The input acoustic signal was generated by an Altec Lansing computer speaker (Model No. ACS 340). The frequency range of this speaker is 30 Hz to 20 kHz. The sensor was measured in a frequency range of 1k Hz to 20 kHz by using sinusoidal sound signals generated by a function generator. The amplitude of the sinusoidal signal is 100 mV. The reflected signal from the sensor was sent to an oscilloscope (Tektronix DPO 7254) via a photodiode and a photodiode current large dynamic range amplifier (Melles Griot). The amplifier converts current signals to a voltage while maintaining a constant zero bias across the detector independent of the signal amplitude. There are nine gain settings available ranging from 1 GΩ to 10 Ω. This permits accurate detection of signals from as low as 1 pA to 100 mA. The maximum detection frequency is 45 kHz, higher than the maximum frequency to be measured.

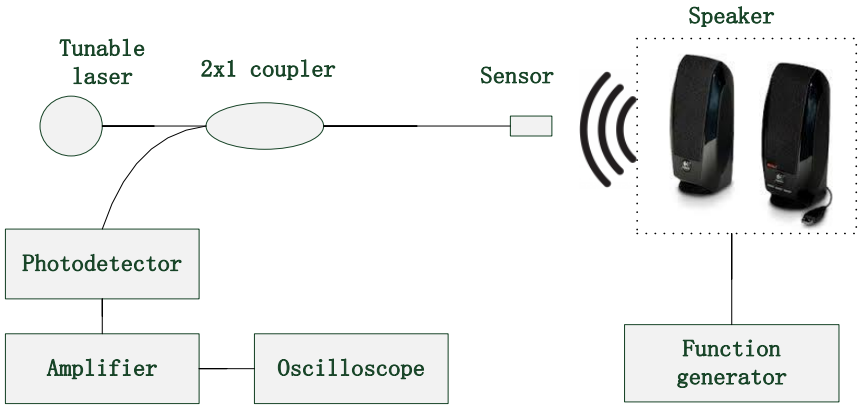

Figure 5.2 Schematic of fiber acoustic sensor as microphone

Representative results at 500 Hz and 4 kHz are shown in Fig. 5.3 and 5.4. The results demonstrate the applicability of the sensor in this frequency range. From the FFT result, the sensor signal frequency is the same as the input signal frequency.

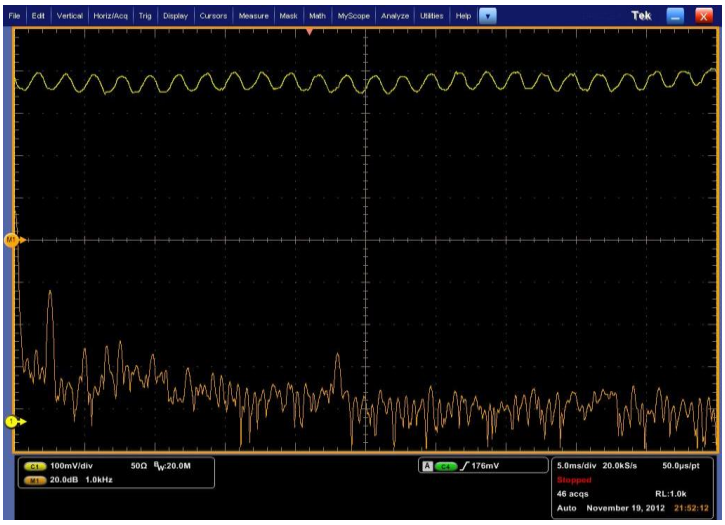

Figure 5.3 Acoustic sensor response to 500 Hz sinusoidal signal

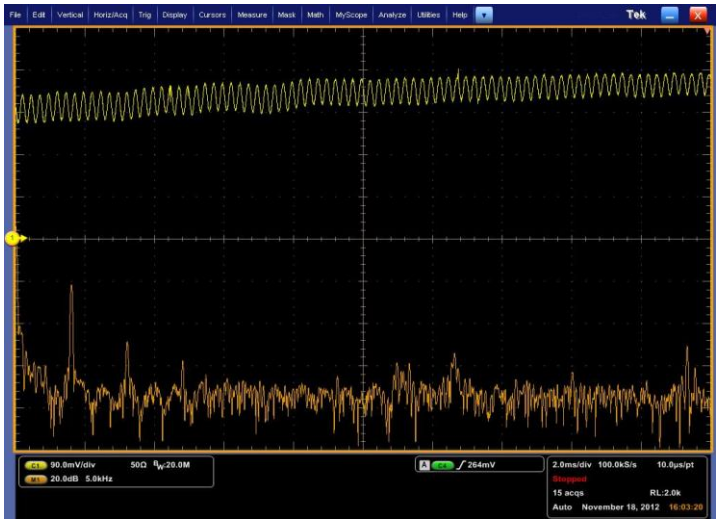

Figure 5.4 Acoustic response to 4 kHz sinusoidal signal

The sensor frequency response curve is plotted in Fig. 5.5, in frequency range of 1 kHz to 20 kHz. The amplitudes of the sensor response signals at different frequencies are close to constant. This is because the resonance frequency of the sensor is in MHz range, so 1 kHz to 20 kHz frequency range is in the linear response region of the sensor.

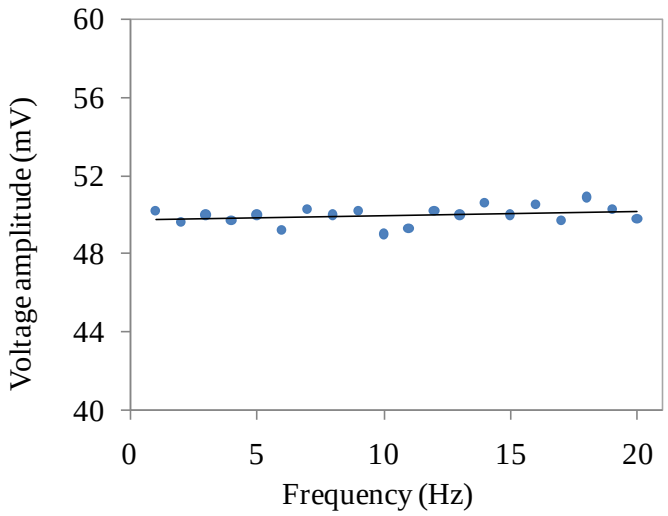

Figure 5.5 Sensor frequency response curve in 1-20 kHz

The sensitivity of an acoustic sensor is obtained by comparing the response of the sensor to a reference microphone/hydrophone. Because there is no reference microphone/hydrophone available, so we define the sensitivity to be the ratio of sensor response voltage to the input acoustic signal voltage.

With an input voltage of 1V, the sensor has a peak-peak output voltage of 50 mV. Considering an amplification ratio of 1000, the sensitivity is 0.005%.

5.3.2. Sensor Test In Water. Fig. 5.6 shows the experiment setup for fiber optic hydrophone measurement. The measurement was carried out in a water tank. An ultrasound transducer (Olympus V326-SU) driven by a high-voltage pulser/receiver (JSR Ultrasonic DPR300) was used as the acoustic source. The transducer was mounted on a three-dimensional translation stage. A fiber acoustic sensor was fixed using a fiber holder (Newport FPH-S) with the fiber axis parallel to the transducer axis. A wavelength tunable laser (HP/Agilent 8168F) was used as light source, and its wavelength was tuned to the operating point in the sensor's interference spectrum to obtain maximum sensitivity. The sensor signal was converted to electrical signal using Tektronix P6073B O/E converter (DC-1.2 GHz), and then connected to Channel 1 in the oscilloscope (Tektronix DPO7254). The pulse-echo signal received by the pulser/receiver was connected to Channel 2 in the oscilloscope. And the internal trigger of the pulser/receiver was

connected to oscilloscope as trigger signal. The signals were averaged 50 times to reduce white noise. To reduce sound reflections from the walls of water tank, acoustically absorbing plastic foams were attached to the inner walls.

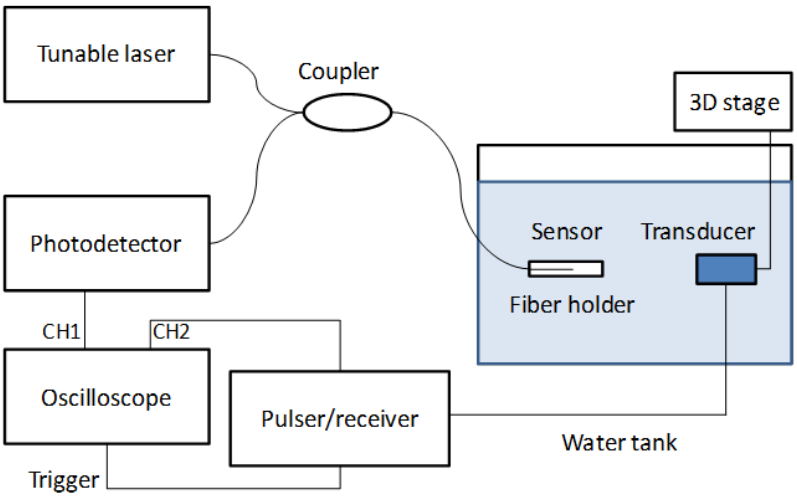

Figure 5.6 Fiber optic hydrophone measurement system

Fig. 5.7 shows the pulse-echo mode operation of the pulser/receiver. The pulse-echo signal connected to channel 2 was used as a reference. From the time of flight between the pulse-echo signal and the sensor output signal, the distance between the transducer and the fiber sensor can be calculated. This helps to identify the sensor's location.

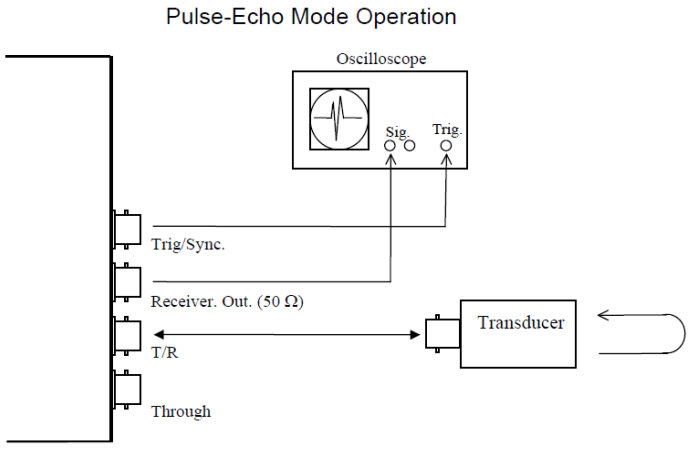

Figure 5.7 Fiber optic hydrophone measurement system

Fig.5.8 displays typical time domain and frequency domain signals of the fiber optic hydrophone. The time domain signal is an exponentially decreasing ringing signal typical to the impulse response of a diaphragm based EFPI sensor. The fundamental resonant frequency f_0 of the sensor is ~6.2 MHz. The thickness and diameter of the sensor's diaphragm are set to be 5 μm and 70 μm respectively. Using Eq. (2.8) and (2.9), we can calculate f_0 to be 6.3 MHz, which is close to the measured result.

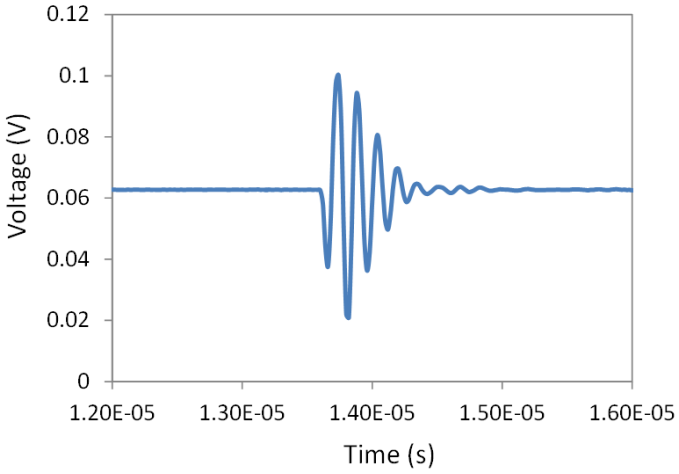

(a)

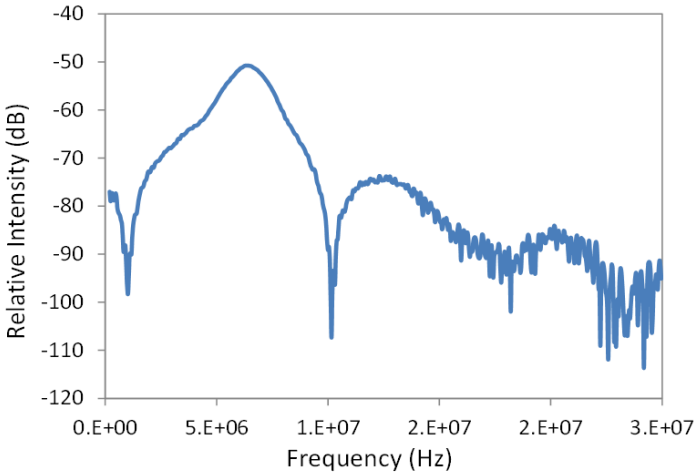

(b)

Figure 5.8 (a) Time-domain response (b) Frequency-domain response of fiber optic hydrophone

The sensitivity of this sensor is calculated as the ratio of peak to peak output voltage (0.08 V) to the ultrasound pulse voltage (100 V). The result is 0.08%.

The frequency responses of the sensor at different incident angles were measured using the setup in Fig. 5.9. The sensor was fixed in a fiber holder mounted on a rotation stage that can rotate 360° with a resolution of 1°. The angle between the transducer and sensor was manually controlled by the rotation stage. The tip of the sensor was placed one inch (focal length of the transducer) away from the ultrasound transducer. The position of the sensor tip was kept constant to avoid measurement error.

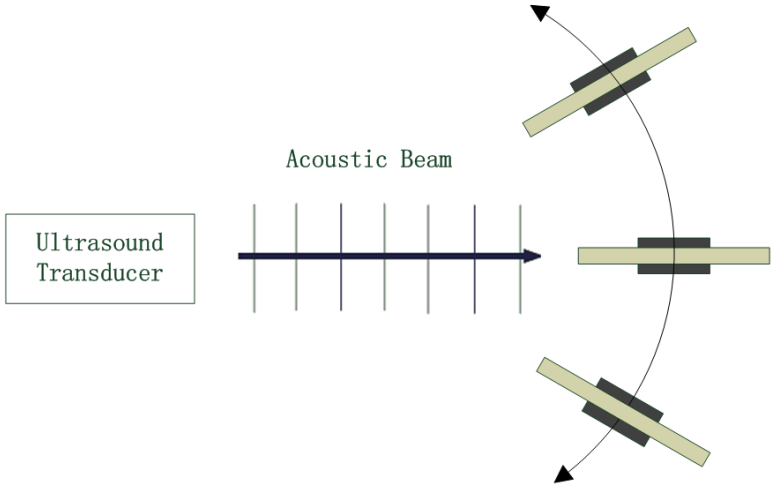

Figure 5.9 Experiment setup for directional response measurement

Fig. 5.10 shows the amplitude frequency response of the sensor at different incident angles, from 0˚ to 90°. With the help of a three-dimensional stage, the sensor was aligned such that its tip remained at the same position when it was rotated. The directional response was obtained by measuring the sensor signal at each rotation angle, and taking fast Fourier Transform (FFT) of the signals. In the experiment, sensor signals were recorded every 10°. The result of rigid piston model at 5 MHz is also plotted in Fig. 5.10. From the figure it can be seen the curve of experiment data follows the same trend as rigid piston model, but the value is smaller than the model.

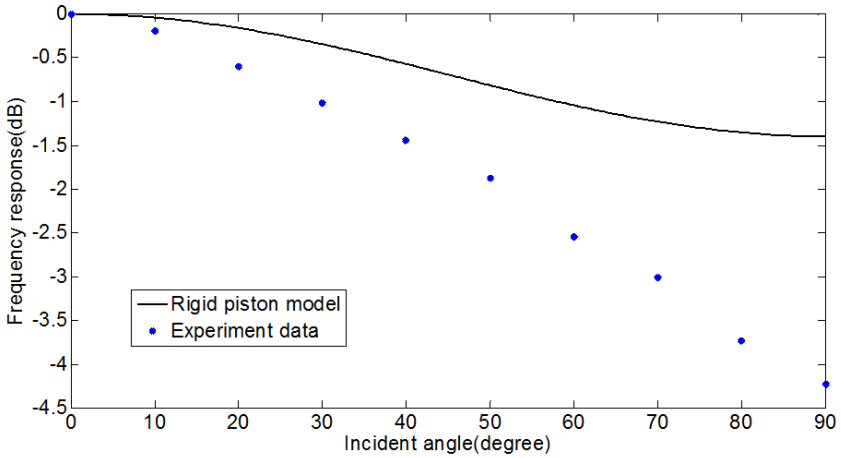

Figure 5.10 Directional response of bare sensor compared with rigid piston model

The signal to noise ratio (SNR) is the difference of power spectrum density between the peak signal and the noise floor. From Fig. 5.8 (b), the SNR is ~25 dB.

The sensor was measured over a range of acoustic pressures by variation of the pulse voltage in the pulser/receiver. The result, shown in Fig. 5.11, shows an excellent linearity of response.

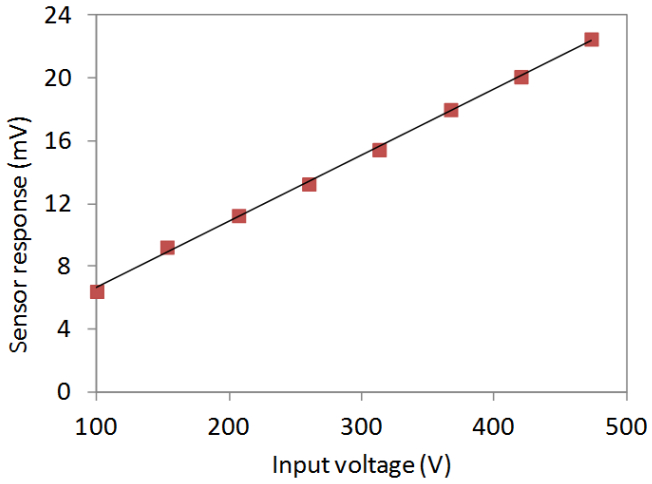

Figure 5.11 Fiber acoustic sensor output as a function of pulse voltage

Adequate stability is necessary for a practical measurement device. The usual source of sensitivity fluctuations is due to environmentally induced variations in the phase bias. The sensitivity over a period of 2.5 hrs is shown in Fig. 5.12. The figure shows the sensor is stable, within the uncertainty of measurement, and over the 2.5 hrs the output does not fluctuate by more than 0.6%. This stability indicates a low sensitivity to ambient temperature and refractive index fluctuations.

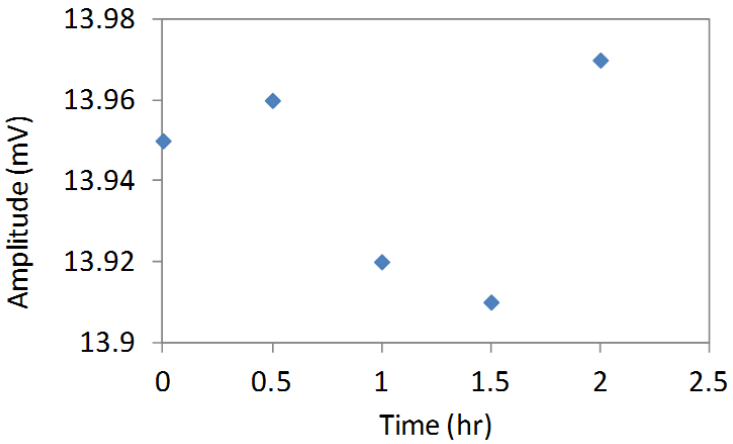

Figure 5.12 Fiber acoustic sensor stability

5.4. ULTRASOUND FIELD CHARACTERIZATION

The sensor was used to characterize the ultrasound field from an ultrasound transducer (Olympus V326-SU). The sound field of a transducer is divided into two zones: the near field and the far field, as shown in Fig. 5.13. There are a number of sound field parameters that are useful in describing the characteristics of a transducer. Knowledge of the beam width and focal zone may be necessary in order to determine whether a particular transducer is appropriate for a given inspection. A transducer's sensitivity is affected by the beam diameter at the point of interest. The smaller the beam diameter, the greater the amount of energy is reflected by a flaw.

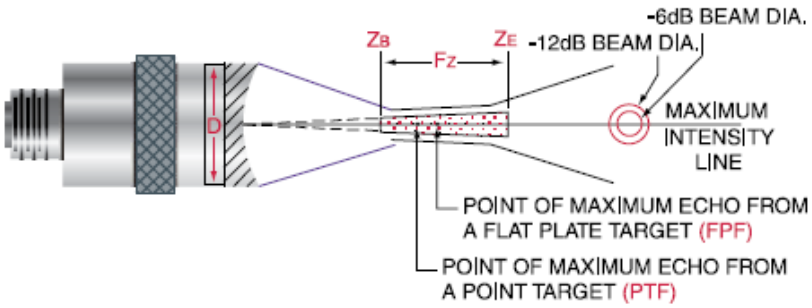

Z_B = Beginning of the Focal Zone
F_z = Focal Zone
Z_E = End of the Focal Zone
D = Element Diameter

Figure 5.13 Ultrasound transducer schematic

Fig. 5.14 plots the result of transducer beam diameter measurement. The fiber sensor was placed at the focal point and moved along the lateral direction. Voltage amplitude of sensor output signal was measured. From the figure, the 3-dB bandwidth of beam diameter is approximately 1.25 mm.

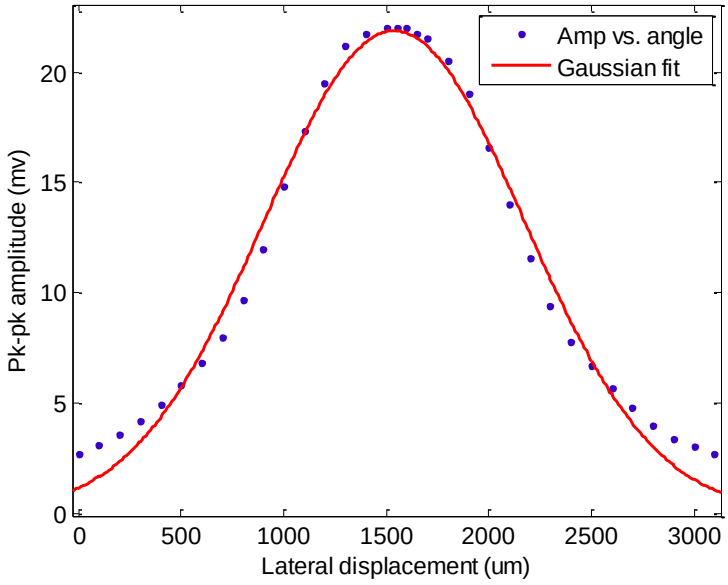

Figure 5.14 Acoustic sensor beam diameter measurement

The sensor was then moved along its fiber axis to measure the focal zone of the trasducer. The result is plotted in Fig. 5.15. The length of focal region is estimated to be 1 cm.

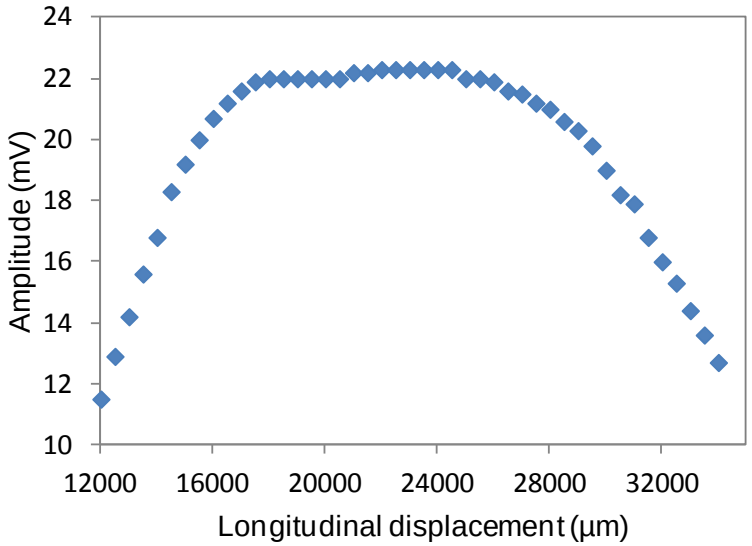

Figure 5.15 Acoustic sensor focal length measurement

5.5. IMPROVEMENT ON SENSOR DIRECTIVITY

Fig. 5.16 shows the sensor packaging method to improve directivity. The sensor head was packaged in a hollow silica tube. The inner diameter of the tube was tapered to ~130 μm. The tube was then coated with wax film by solidifying liquid wax uniformly at the surface of silica tube. Wax is a sound wave absorbing material like plastics and silicon rubbers [61]. It was chosen as coating material because of its low cost and easy for operation. A short distance (tens of micro meters) was kept from the sensor diaphragm to the tube endface for protection purpose. Finally epoxy was applied to bond the lead-in fiber to the encapsulating tube.

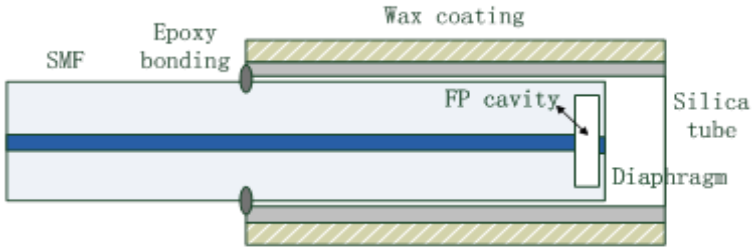

Figure 5.16 Directional response of packaged sensor

Due to its acoustic absorbing property, the wax film absorbs incident acoustic waves impinging on its surface. When the sensor was placed at zero degree to the acoustic source, no waves are absorbed. As the inclination angle θ increases, some waves got absorbed by the wax film. Therefore, the amount of acoustic waves reaching the diaphragm decreases, and the sensor becomes more directive.

Fig. 5.17 plots the directional response of the packaged sensor.

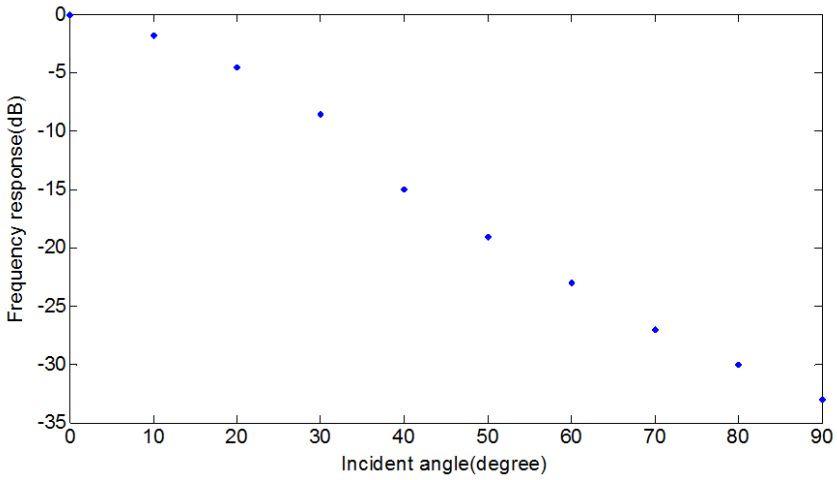

Figure 5.17 Directional response of packaged sensor

Comparing Fig. 5.10 and Fig. 5.17, the amplitude of sensor's frequency response decreases much faster after packaging. 3-dB bandwidth of frequency response changes from ~70˚ to ~8˚. It proves the functionality of this packaging method to increase sensor directivity.

5.6. ACOUSTIC SENSOR WITH CORRUGATED DIAPHRAGM

As discussed in section 2, with a corrugated diaphragm the sensor may achieve a balance between sensitivity and bandwidth. Experiment was conducted to test the performance of a corrugated diaphragm.

The diaphragm has a total thickness of 10 μm and diameter of 70 μm. A circular hole, with diameter of 50 μm and thickness of 5 μm, was fabricated at the center of the diaphragm with fs laser.

Fig. 5.18 plots the time-domain and frequency-domain response of this diaphragm to ultrasound signal.

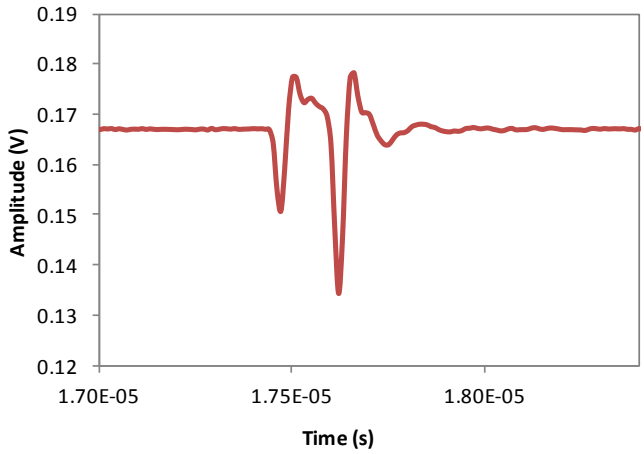

(a)

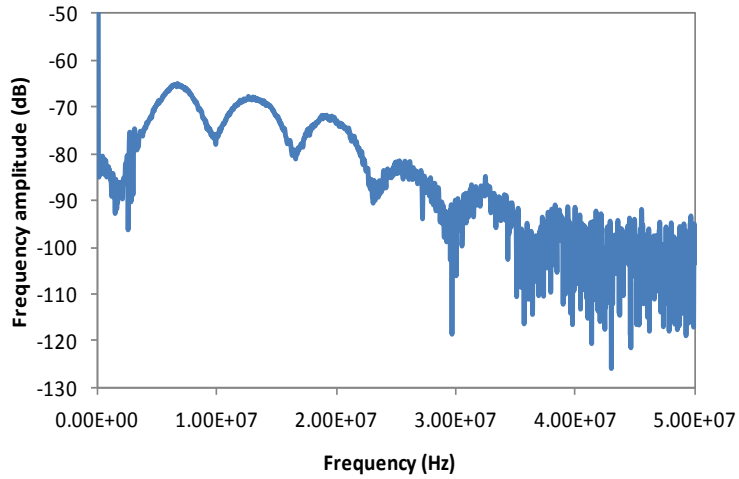

(b)

Figure 5.18 (a) Time domain (b) frequency domain response of corrugated diaphragm

From Fig. 5.18, the sensor response is different from the response of plane diaphragm. The maximum peak to peak voltage is 0. 05mV. The sensor has lowest resonance frequency at ~7 MHz, and higher mode resonance frequencies at 12, 18 MHz. Comparing the result to the plane diaphragm, the corrugated diaphragm helps to increase the resonance frequency while maintaining a relatively high sensitivity.

5.7. SUMMARY

In this section, the fs laser fabricated EFPI sensor was investigated for acoustic sensing. The sensor was tested for low frequency acoustic signals in air and high frequency ultrasound signals in water. The acoustic characteristics, including sensitivity, resonance frequency and angular dependence were measured and analyzed. The linearity and stability of the sensor for ultrasound measurement were provided. The angular dependence of the sensor falls between rigid baffled model and unbaffled model. A sensor packaging method was proposed and demonstrated to improve the directivity of the sensor. Diaphragm with corrugated structure was tested for ultrasound sensing, and the result indicates a larger bandwidth with relatively high sensitivity. Interpretation of the output signals needs to be further explored.

6. SIMULTANEOUS PRESSURE AND TEMPERATURE TEST

6.1. REVIEW OF CURRENT METHODS

Pressure and temperature are two important parameters in well and reservoir monitoring [62]. Accurate, continuous and real time data of pressure and temperature helps in oil and reservoir management. Sensors with dual parameter sensing capability and survivability in the down-hole harsh environment are necessary in such applications. Fiber optic sensors, with advantages such as small size, high sensitivity, resistance to harsh environment and multiplexing capability, are the best candidates for pressure and temperature down-hole monitoring.

In the past years, several types of fiber optic sensors have been demonstrated for pressure and temperature sensing. The major types include fiber Bragg Grating (FBG) for temperature or dual parameters measurement [63-66], diaphragm based Fabry-Perot interferometer (FPI) for pressure sensing [67, 68], long period fiber grating (LPFG) for temperature sensing [69], etc. An early reported type used a single FBG that was half encapsulated and the other half fixed in a polymer filled metal cylinder [63]. Since the resonance wavelength shift of FBG is affected by temperature and pressure both, the cross sensitivity becomes a problem. Double FBG coated by a special polymer in a metal tube was later developed to discriminate pressure and temperature effect. FBGs in specialty fibers have also been proposed, i.e., FBGs in standard and grapefruit microstructure fibers (GMF) [70]. However, FBG has a maximum temperature limit of ~300 ˚C. Recently, a combined pressure-temperature sensor consisting of two low-finesse Fabry-Perot resonators was reported [71]. This structure provides potentials for high-temperature applications.

6.2. IFPI FOR TEMPERATURE SENSING

The temperature sensitivity of an IFPI is contributed by thermo-optic and thermal-expansion effects,

$$K_T = (\alpha_{TO} + \alpha_{CTE})\lambda_v \tag{6.1}$$

where α_{TO} is the thermo-optic coefficient, α_{CTE} is the thermal expansion coefficient, and λ_V is the wavelength of an interference valley. For fused silica the typical values are α_{TO} = 8.3×10^{-6} °C^{-1} and $\alpha_{CTE} = 5.5 \times 10^{-7}$ °C^{-1}, respectively [72], so in an IFPI thermo-optic effect plays a major role in its temperature sensitivity.

6.3. SENSOR FABRICATION

The proposed sensor consists of a pair of cascaded IFPI and EFPI, as shown in Fig.6.1 (a). The IFPI is formed by two internal partial reflectors created in the core of a single-mode fiber. The thermal modulation of the refractive index of fiber core provides temperature sensing function of IFPI. The EFPI is located at the tip of the fiber, formed by the fiber endface and a thin silica diaphragm which deflects under pressure, providing pressure sensing function.

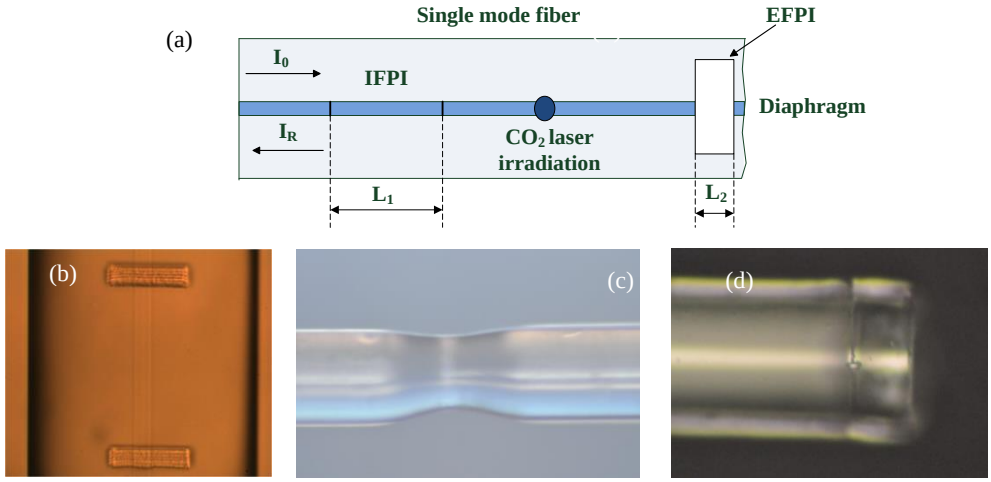

Figure 6.1. (a) Scheme of proposed sensor (b) photo of IFPI (c) photo of CO2 laser irradiation (d) photo of EFPI

Sensor fabrication consists of the following steps. First, EFPI was fabricated at the tip of a single mode fiber. A section of hollow core silica tube (TSP075150, Polymicro Inc.) was spliced to a standard single-mode fiber (Corning SMF-28e). Then the tube was cleaved at a distance (tens of micrometers) from the splice point with the help of a microscope. The tube was then spliced to another SMF to form a sealed air cavity in between two fibers. Precision fiber cleaving was applied to cut the fiber so that a thin piece of fiber was left to perform as the diaphragm. Finally the as-cleaved diaphragm

was thinned and roughened by fs laser (Coherent RegA 9000, 200 fs pulse duration, 250 kHz repetition rate and 800 nm central wavelength).The fs laser micromachining method was described in section 3. Fig. 6.1(d) shows the image of an EFPI fabricated with this method.

Next, IFPI was fabricated at a short distance (~1 cm) from the EFPI. It was created by inscribing two parallel lines in the fiber core with fs laser. A water immersion lens (Olympus UMPlanFL 20X) was used to focus the fs laser into the fiber core. Fig. 6.1(b) shows the microscopic image of an IFPI. The two parallel lines in fiber core are clearly visible.

With the above fabrication procedure, IFPI with length L_1 of a few hundred micrometers and EFPI with length L_2 of tens of micrometers were successfully produced. L_1 was set to be significantly longer than L_2 to facilitate signal processing which will be discussed later.

The refractive index change in the fiber core induced by fs laser is very small ($10^{-4} – 10^{-2}$) [73], therefore the reflectivity of internal reflectors in an IFPI is far lower than the reflectivity of an air/glass interface in an EFPI (4%). Due to the unbalanced reflectivity, there is a substantial difference in the power levels of EFPI and IFPI interference signals. The power level of IFPI signal is so low that it cannot be observed in the spectrum.

One method to balance the power levels of IFPI and EFPI signals is to add transmission loss between IFPI and EFPI. In this paper, a CO_2 laser (SYNRAD, Inc.) with a free space wavelength of 10.6 μm was employed to heat the fiber to increase light loss. Fig. 6.2 and 6.3 show the photo and diagram of CO_2 laser irradiation system. A ZnSe cylindrical lens with a focal length of 50 mm was used to shape the CO_2 laser beam into a narrow line with a line width of around 220 μm [74]. The CO_2 laser was controlled by a computer so that the output power and exposure duration could be accurately adjusted. During fabrication, the CO_2 laser heated the fiber and created a micro bend between EFPI and IFPI. With laser output power of ≥12 W, and irradiation time of ≥ 400 ms, the fiber reflection loss increases by ~20-30 dB. An optical spectrum analyzer (Ando AQ 6319) was used to monitor the reflection spectrum. The CO_2 laser parameters are adjusted in-situ to obtain spectrum with distinct multiplexed signals.

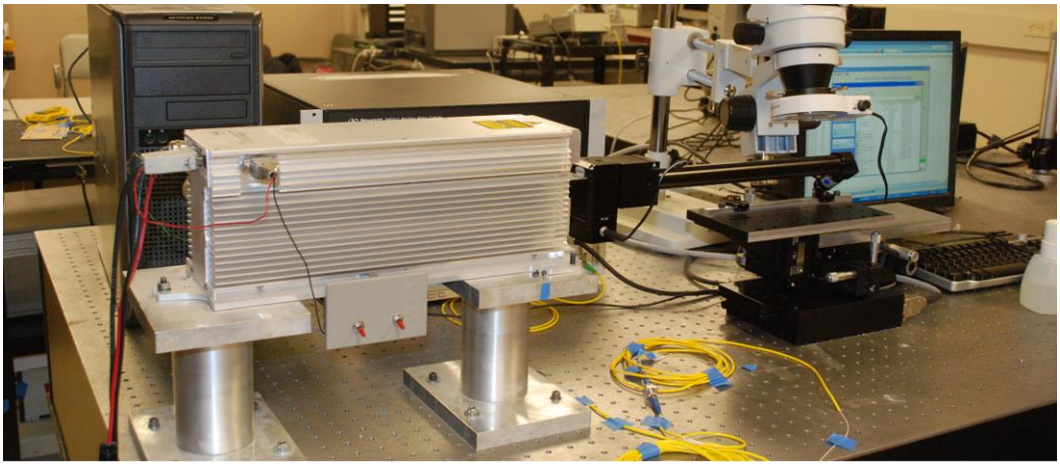

Figure 6.2 Photo of CO_2 laser irradiation system

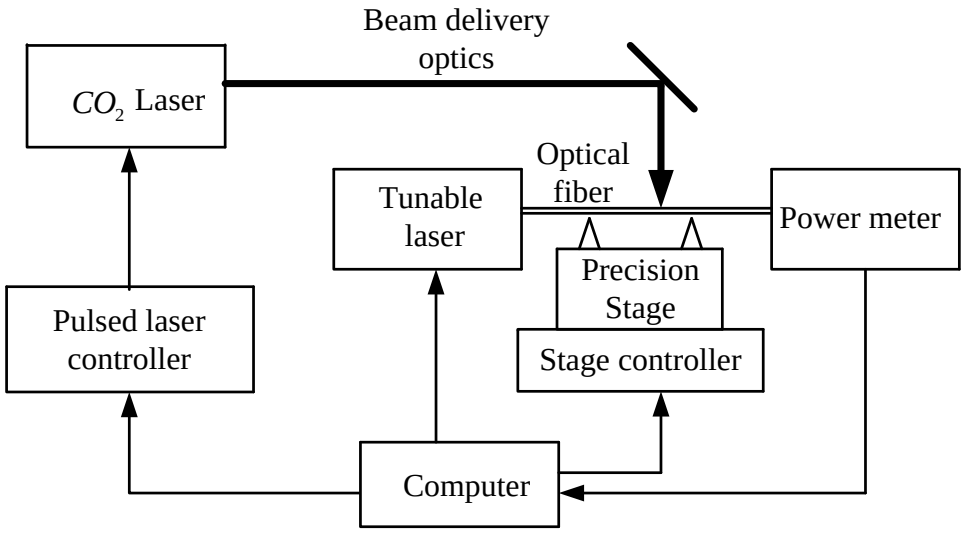

Figure 6.3 Diagram of CO_2 laser irradiation system

6.4. SIGNAL PROCESSING

When temperature and pressure changes are simultaneously applied, the wavelength shifts in IFPI and EFPI can be expressed as

$$\Delta\lambda_{IFPI} = K_{P,IFPI} * \Delta P + K_{T,IFPI} * \Delta T \quad (6.2)$$

$$\Delta\lambda_{EFPI} = K_{P,EFPI} * \Delta P + K_{T,EFPI} * \Delta T \quad (6.3)$$

Temperature and pressure can be obtained by solving the following matrix

$$\begin{bmatrix} \Delta T \\ \Delta P \end{bmatrix} = \frac{1}{\Omega} \begin{pmatrix} K_{P,EFPI} & -K_{P,IFPI} \\ -K_{T,EFPI} & K_{T,IFPI} \end{pmatrix} \begin{bmatrix} \Delta_{\lambda,IFPI} \\ \Delta_{\lambda,EFPI} \end{bmatrix} \tag{6.4}$$

where $\Omega = K_{P,EFPI}K_{T,IFPI} - K_{T,EFPI}K_{P,IFPI}$

The fast Fourier Transform (FFT) is a widely used method to demodulate multiplexed Fabry Perot interferometer (FPI) signals. By taking Fourier transform of the interferogram, the optical path difference (OPD) of each FPI can be obtained. The minimum detectable OPD change is given by

$$\Delta l = \frac{\pi}{\nu_E - \nu_S} \tag{6.5}$$

where ν_E and ν_S are the smallest and largest wavenumbers in the measurement range, respectively.

According to Eq. (6.5), for a broadband light source with wavelength range from 1520 nm to 1620 nm, Δl is approximately 12 μm. Due to the low resolution, FFT is not suitable for signal demodulation when the cavity length change is small. Recently, a fast-Fourier-transform-based wavelength tracking method to demodulate multiplexed IFPI signals was proposed [75]. This method uses band-pass filters to extract specific frequency components and transform them back to wavelength domain, and then use wavelength tracking method to find OPD change. Demodulation accuracy has been improved with this method.

Fig. 6.4(a) plots a typical spectrum of multiplexed IFPI and EFPI sensors, and Fig. 6.4(b) plots the FFT of the spectrum. Two main frequency components with substantially different cavity lengths can be clearly seen, corresponding to EFPI and IFPI. The OPD for IFPI is n (n = 1.4682) times the actual cavity length, so the cavity lengths of EFPI and IFPI in this sensor are 62 μm and 680 μm, respectively.

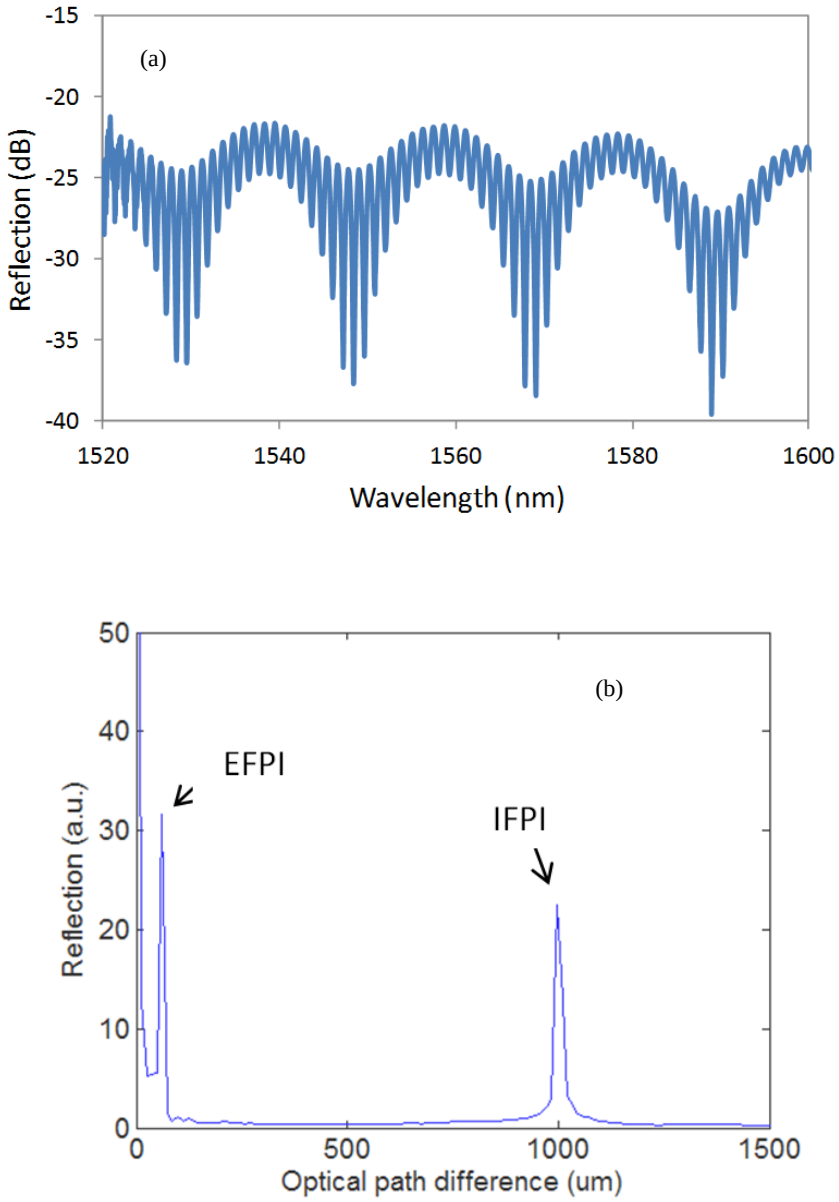

Figure 6.4 (a) Spectrum of multiplexed EFPI and IFPI sensors (b) FFT of the multiplexed sensor spectrum

Two Hamming-windowed digital filters were used to select each frequency component. The filters are plotted in Fig. 6.5 in different colors.

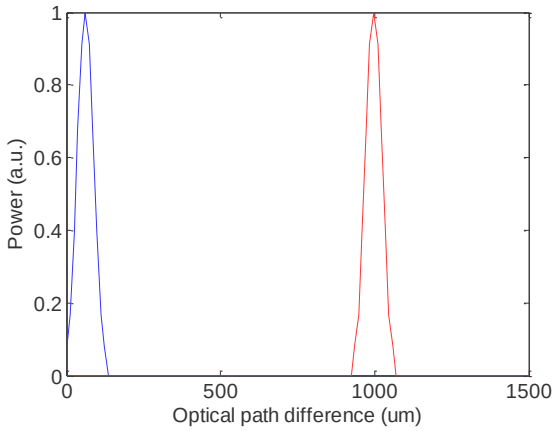

Figure 6.5 Hamming windowed digital filters

After filtering, interference spectrum was reconstructed using IFFT. Fig. 6.6 and 6.7 plot the selected frequency component and reconstructed waveform for EFPI and IFPI, respectively.

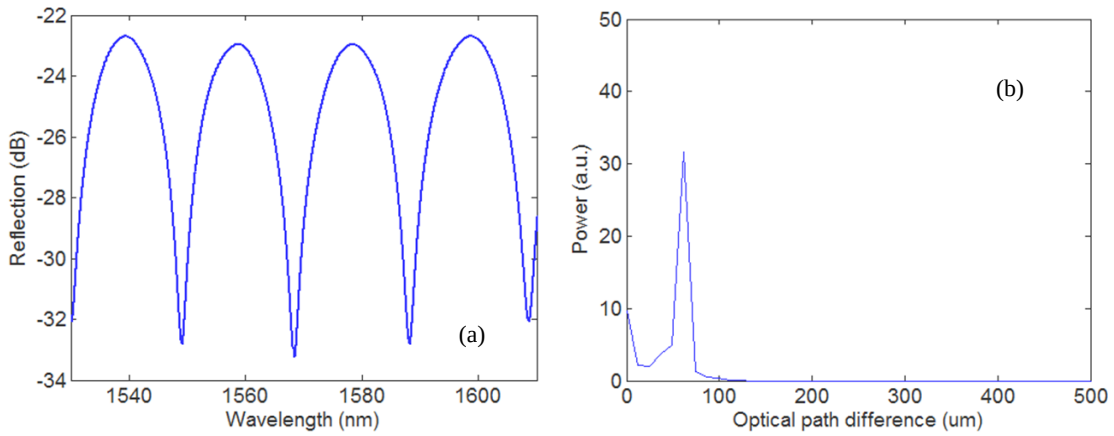

Figure 6.6 (a) Frequency spectrum of EFPI sensor after filtering (b) Inverse FFT result of the frequency spectrum

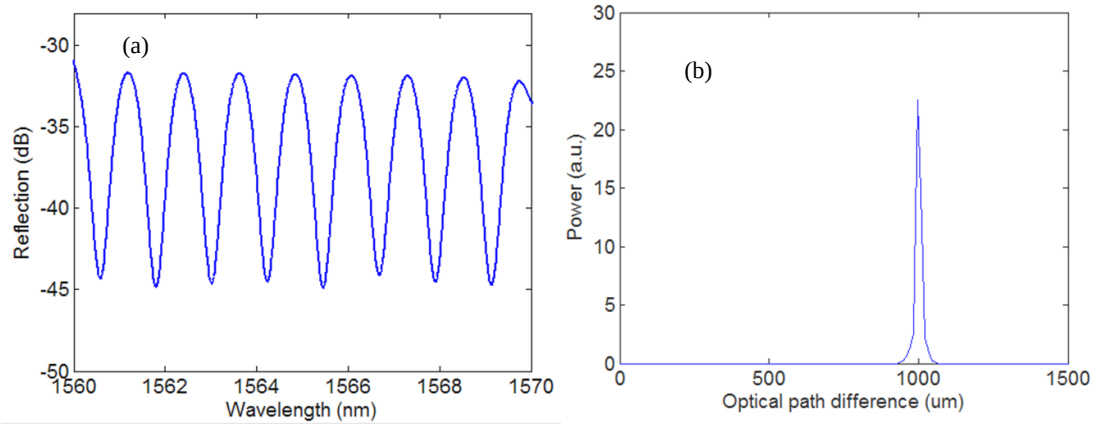

Figure 6.7 (a) Frequency spectrum of IFPI after filtering (b) Inverse FFT result of the frequency spectrum

One interference valley in the reconstructed waveform was chosen as the tracking wavelength. Then wavelength tracking method can be used to obtain wavelength shift. The rest of the signal processing is the same as conventional method described in section 2.

6.5. EXPERIMENTS AND RESULTS

The experiment setup for sensor characterization is illustrated in Fig. 6.8. In the measurement, a 100 nm bandwidth ASE light source (BWC-ASE) was launched into the sensor via a 3-dB fiber coupler. The sensor was sealed in a Swagelok tube acting as pressure gauge where the air pressure was supplied using a compressed Argon gas cylinder and controlled by a pressure controller (MKS640). The pressure controller/generator can supply a static pressure up to 6.895×10^5 Pa with a precision of ~0.5%. The Swagelok tube was then placed in a high temperature furnace (Lindberg/ blue M), which could provide temperature up to 1100 °C with programmable temperature steps. The sensor output signal was recorded using an optical spectrum analyzer (Ando AQ6319).

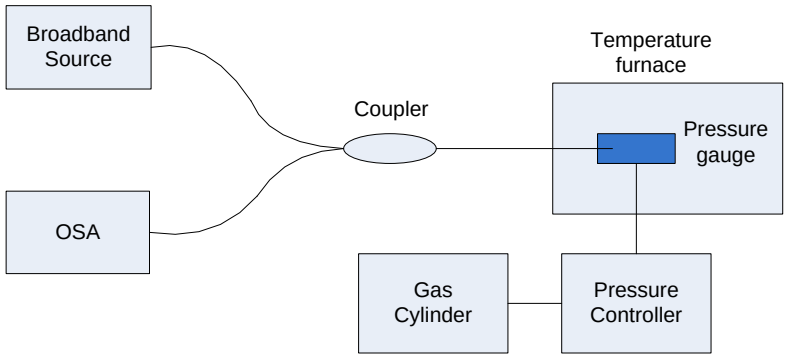

Figure 6.8 Experiment setup for temperature and pressure measurement

First, the temperature and pressure sensitivities for each sensor were initially calibrated. The temperature sensitivity was tested at zero pressure, and the pressure sensitivity was tested at room temperature (~20 °C). The results are presented in Fig. 6.9 and 6.10.

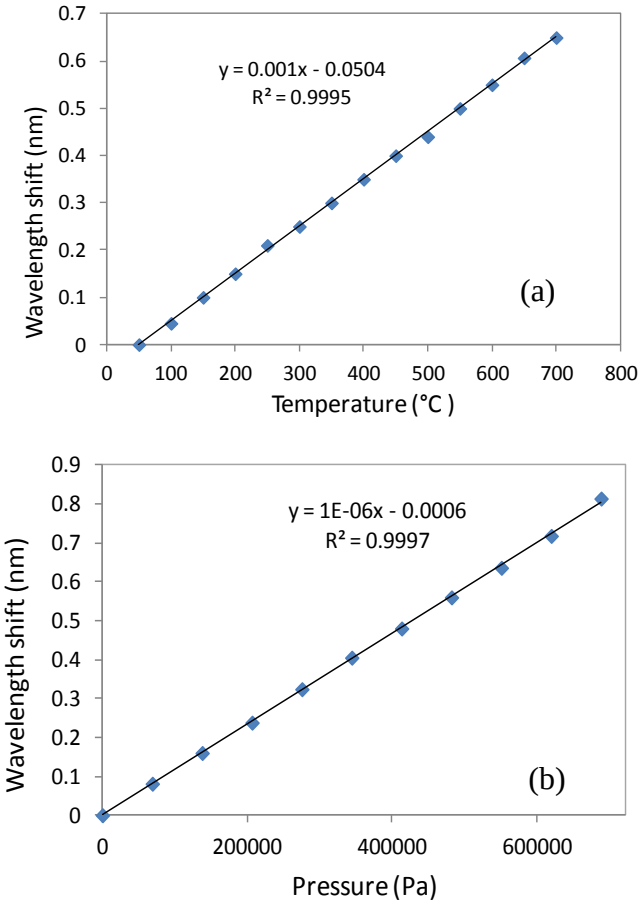

Figure 6.9 (a) Temperature response of EFPI (b) Pressure response of EFPI

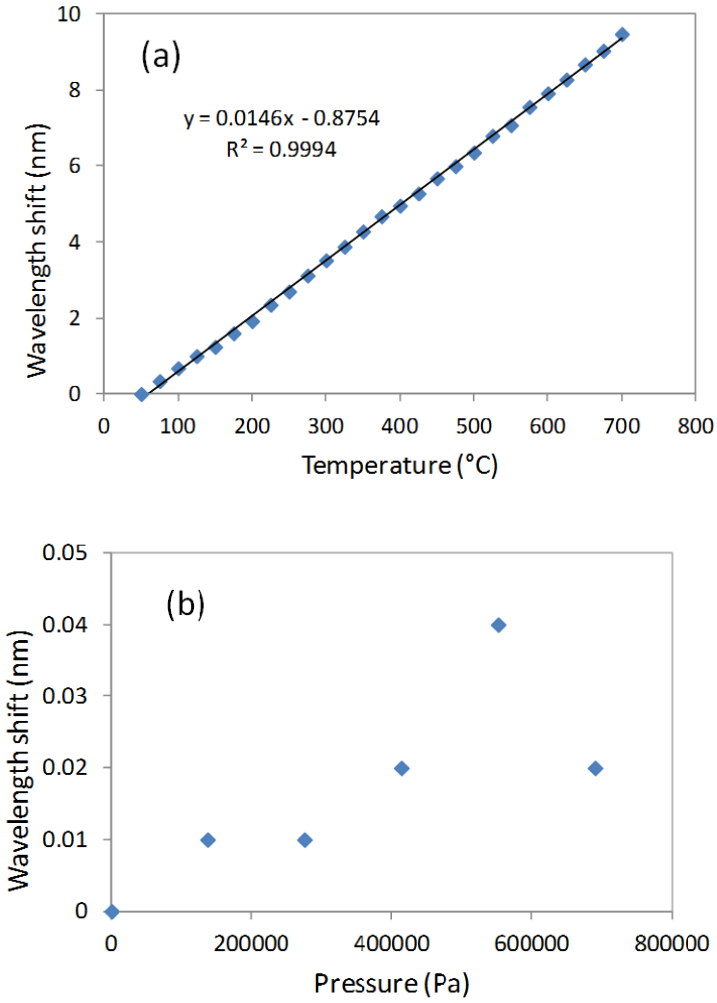

Figure 6.10 (a) Temperature response of IFPI (b) Pressure response of IFPI

From the results, the K coefficients in Eq. (6.2) and (6.3) could be obtained. The values are listed in Table 6.1.

Table 6.1 Calibration results

Coefficient	$K_{T,EFPI}$	$K_{P,EFPI}$	$K_{T,IFPI}$	$K_{P,IFPI}$
Value	0.001 nm/°C	1×10^{-6} nm/Pa	0.0146 nm/°C	0

Then Eq. (6.5) could be written as

$$\begin{bmatrix} \Delta T \\ \Delta P \end{bmatrix} = \frac{1}{1.46\times10^{-8}} \begin{pmatrix} 1\times10^{-6} & 0 \\ -0.001 & 0.0146 \end{pmatrix} \begin{bmatrix} \Delta_{\lambda,IFPI} \\ \Delta_{\lambda,EFPI} \end{bmatrix}$$

Next, the sensor was tested for simultaneous pressure/temperature measurement. The measurement procedure was as follows. Given a constant temperature, the pressure was increased from 0 Pa to 6.895×10^5 Pa at per increment of 1.379×10^5 Pa. The temperature was set to increase from room temperature (20 °C) to 700 °C at increments of 50 °C. The measured data were analyzed using the above mentioned demodulation method.

Fig. 6.11 plots applied pressure and measured pressure at various temperatures. Fig. 6.12 plots applied temperature and measured temperature at various pressures. From these figures it can be seen that measured results fit well with set temperature and pressure.

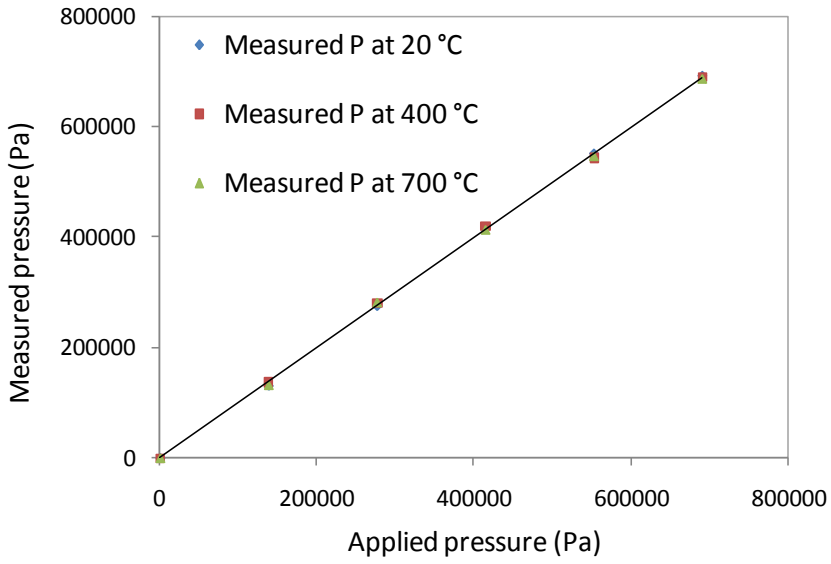

Figure 6.11 Applied pressure and measured pressure

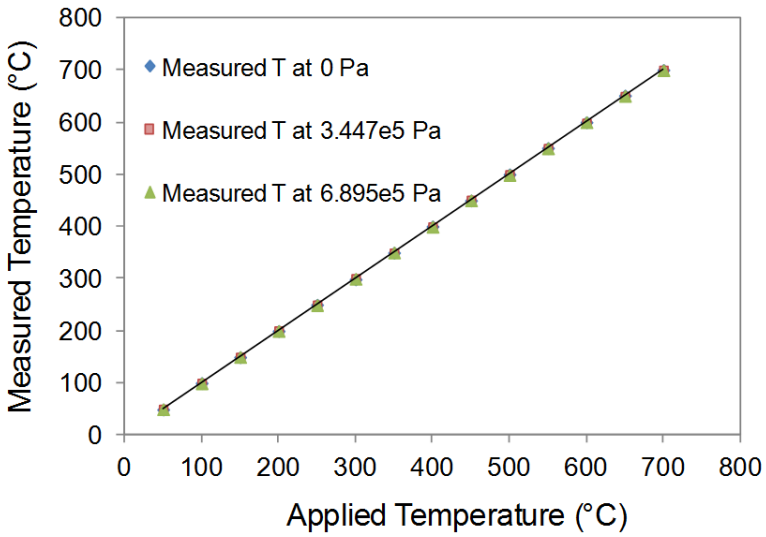

Figure 6.12 Applied temperature and measured temperature

6.6. SUMMARY

In this section, a miniature, all-fiber IFPI/EFPI sensor suitable for simultaneous measurement of temperature and pressure was described. The sensors were fabricated with the help of fs laser micromachining. The IFPI and EFPI signals were unambiguously separated using band pass filtering of frequency spectrum. The sensor was tested up to 700 °C and 6.895×10^5Pa, and the results show good linearity in the measurement range, providing potential for down-hole measurements at high temperature and pressure environments.

7. SUMMARY AND FUTURE WORK

7.1. BRIEFLY SUMMARIZE THE DISSERTATION WORK

Motivated by the needs for pressure/acoustic sensing in harsh environment applications, this work focuses on design, development and demonstration of miniaturized fiber sensor probes through fs laser fabrication.

The scope of the dissertation work consists of device design, device modeling/simulation, laser fabrication system setups, signal processing method development, and sensor performance evaluation and demonstration.

The principles of diaphragm based EFPI sensors for static and acoustic pressure measurement are analyzed. Three dimensional ANSYS model of plane and corrugated diaphragms were built. By using static, modal and harmonic analysis functions in ANSYS 7.0, we obtain the deformation, modal solution and frequency response of the sensor. The angular dependence of the frequency response was also modeled using ANSYS.

The fs laser setup and sensor fabrication procedure was described in details. The advantages of fs laser micromachined sensors were discussed. Current issues with fs laser machining were also discussed.

Thin diaphragms with thicknesses as small as 2.6 μm are achievable. A pressure sensitivity of 2.8×10^{-4} nm/Pa and a resolution of 180 Pa were demonstrated. The sensors have been tested at high temperatures up to 700 °C, showing a linear response to temperature with low temperature sensitivity of 5.57×10^{-7}/°C, corresponding to a small pressure-temperature cross sensitivity less than 15.86 Pa/˚C. The sensor has also been demonstrated for measurement of autogenic pressures of water vapor up to 200 ˚C. Without temperature compensation, the pressure measurement results agreed well with those calculated based on the theoretical model.

The acoustic characteristics, including sensitivity, resonance frequency and angular dependence of EFPI sensors were measured and analyzed. The linearity and stability of the sensor for ultrasound measurement were provided. The angular dependence of the sensor falls between rigid baffled model and unbaffled model. A sensor packaging method was proposed and demonstrated to improve the directivity of

the sensor. Diaphragm with corrugated structure was tested for ultrasound sensing, and the result indicates a larger bandwidth with relatively high sensitivity.

Cascaded IFPI and EFPI sensor for simultaneous measurement of temperature and pressure was proposed and demonstrated. The IFPI and EFPI signals were unambiguously separated using band pass filtering of frequency spectrum. The sensor was tested up to 700 °C and 6.895×10^5Pa, and the results show good linearity in the measurement range, providing potential for down-hole measurements at high temperature and pressure environments.

7.2. INNOVATIONS/CONTRIBUTIONS

The major scientific and technical merits of this work include:

1) For the first time, the femtosecond laser micromachining technique was used to fabricate diaphragm based EFPI pressure sensor. With the sub micrometer precision, we can fine tune the sensitivity and pressure range. The unique characteristics of fs laser roughened surface helps to eliminate the effect of environmental refractive index change on the sensor signal. The short air cavity created by fs laser helps to increase fringe visibility and minimize the temperature cross sensitivity. The all silica structure prevents the sensor from being affected by CTE mismatch and makes it more robust for high temperature sensing applications. The sensor survived high temperature up to 700 °C with low temperature cross sensitivity.
2) A novel packaging method to improve the sensor's directivity to ultrasound signals was demonstrated. 3-dB bandwidth of frequency response changes from ~70˚ to ~8˚ with this packaging method. It can also helps to protect the fragile thin diaphragm.
3) A novel corrugated diaphragm structure fabricated by fs laser was simulated and tested. With finite element analysis, the sensitivity and resonance frequency could be predicted and optimized. This structure helps to achieve a balance between the sensitivity and resonance frequency.
4) A novel multi parameter sensor for pressure and temperature simultaneous sensing was demonstrated. The sensor has small size, low cross sensitivity and

high temperature survivability. Pressure and temperature information could be demodulated accurately using improved signal processing method.

7.3. PUBLICATIONS DURING THE DISSERTATION WORK

Papers with asterisk symbol are related to this work.

1*. Y. Huang, T. Wei, Z. Zhou, **Y. Zhang**, G. Chen, and H. Xiao, "An extrinsic Fabry–Perot interferometer-based large strain sensor with high resolution " Meas. Sci. Technol. **21**, 105308 (2010).

2. **Y. Zhang**, Y. Li, T. Wei, L. Xinwei, Y. Huang, G. Chen, and H. Xiao, "Fringe Visibility Enhanced Extrinsic Fabry-Perot Interferometer Using a Graded Index Fiber Collimator," Photonics Journal, IEEE **2**, 469-481 (2010).

3. X. Lan, Y. Han, T. Wei, **Y. Zhang**, L. Jiang, H.-L. Tsai, and H. Xiao, "Surface-enhanced Raman-scattering fiber probe fabricated by femtosecond laser," Opt. Lett. **34**, 2285-2287 (2009).

4. Y. Huang, Z. Zhou, **Y. Zhang**, G. Chen, and H. Xiao, "A temperature self-compensated LPFG sensor for large strain measurements at high temperature", IEEE Transactions on Instrumentation & Measurement, 59 11, 2997-3004, 2010

5. **Y. Zhang**, H. Xiao, T. Wei, X. Lan, H. Duan, "Side-coupled optical fiber devices for sensing applications," SPIE Proceedings, vol. 7682, 2010

6. Y. Huang, G. Chen, H. Xiao, **Y. Zhang** and Z. Zhou, "A quasi-distributed optical fiber sensor network for large strain and high-temperature measurements of structures," SPIE Proceedings vol. 7983, 2011

7. **Y. Zhang**, E. Pienkowski, T. Wei, J. Huang and H. Xiao, "Concentrically symmetric hollow core interferometer for common path optical coherence tomography", 57th IIS conference, 2011

8. **Y. Zhang**, E. Pienkowski, H. Xiao, "Polymer microlens fiber probe for common path optical coherence tomography", SPIE Proceedings, vol. 8213, 82133I, 2012

9. Y. Li, **Y. Zhang**, X. Lan and H. Xiao, "Common-path endoscopic optical coherence tomography application to human internal organs detection," Consumer Electronics, Communications and Networks (CECNet), 2012 2nd International Conference, vol., no., pp.2455-2458, 21-23 April 2012

10*. **Y. Zhang**, L. Yuan, X. Lan, A. Kaur, J. Huang and H. Xiao, "High temperature fiber optic Fabry-Perot interferometric pressure sensor fabricated by femtosecond laser," Optics Letters, Article in Press, 2013

11*. **Y. Zhang**, J. Huang, X. Lan and H. Xiao, "Simultaneous pressure and temperature measurement using IFPI and EFPI sensors," to be submitted, 2013

12*. **Y. Zhang**, X. Lan, J. Huang, A. Kaur and H. Xiao, "Fiber optic ultrasound sensor with improved directivity," to be submitted, 2013

7.4. FUTURE WORK

The future work recommendations are listed below:

1) The surface quality of the FP cavity fabricated by fs laser is desired to be improved to obtain better signal strength. The improvement approaches may include post thermal treatment, high power laser reflow or fine polishing using fs laser with much smaller energy.
2) The signal processing technique employed currently is mainly based on curve fitting. In most cases, researchers are more interested in the relative position of the resonance peak. A waveform cross-correlation technique may be useful to acquire better measurement accuracy and evidently suppress the noise signal.
3) Investigate the long term stability of the fs laser fabricated pressure sensor.
4) Investigate distributed pressure sensing techniques using Fabry-Perot interferometer or other types of sensors.
5) Study the physics of acoustic wave and material interaction dynamics. Knowledge of the dynamics will help to understand and predict acoustic sensor performance.
6) Design corrugated diaphragm structures to optimize the sensor performance.
7) Investigate the feasibility of using the sensor for other applications, such as partial discharge detection, engine monitoring, acoustic imaging, etc.

BIBLIOGRAPHY

[1] Available: http://en.wikipedia.org/wiki/Pressure, Oct 28, 2013.

[2] N. Instruments. (2011). *Pressure measurement basics*. Available: http://www.ni.com/white-paper/13034/en/

[3] E. Manikandan, K.A. Karthigeyan, and K. I. A. James, "Micro Electro Mechanical System (MEMS) based Pressure Sensor in Barometric Altimeter " *International Journal of Scientific & Engineering Research*, vol. 2, 2011.

[4] Y. Ge, M. Wang, and H. Yan, "Optical MEMS pressure sensor based on a mesa-diaphragm structure," *Opt Express*, vol. 16, pp. 21746-52, Dec 22 2008.

[5] W. Hasenkamp, D. Forchelet, K. Pataky, J. Villard, H. Van Lintel, A. Bertsch, *et al.*, "Polyimide/SU-8 catheter-tip MEMS gauge pressure sensor," *Biomed Microdevices*, vol. 14, pp. 819-28, Oct 2012.

[6] J. W. Wheeler, J. G. Dabling, D. Chinn, T. Turner, A. Filatov, L. Anderson, *et al.*, "MEMS-based bubble pressure sensor for prosthetic socket interface pressure measurement," *Conf Proc IEEE Eng Med Biol Soc*, vol. 2011, pp. 2925-8, 2011.

[7] L. T. Chen, J. S. Chang, C. Y. Hsu, and W. H. Cheng, "Fabrication and Performance of MEMS-Based Pressure Sensor Packages Using Patterned Ultra-Thick Photoresists," *Sensors (Basel)*, vol. 9, pp. 6200-18, 2009.

[8] N. Lagakos, J. H. Cole, and J. A. Bucaro, "Microbend fiber-optic sensor," *Appl Opt*, vol. 26, pp. 2171-80, Jun 1 1987.

[9] W. B. Spillman, Jr., "Multimode fiber-optic pressure sensor based on the photoelastic effect," *Opt Lett*, vol. 7, pp. 388-90, Aug 1 1982.

[10] Y. Yang, J. Li, W. Duan, X. Zhang, W. Jin, and M. Yang, "An embedded pressure sensor based on polarization maintaining photonic crystal fiber," *Meas. Sci. Technol.*, vol. 24, p. 094004, 2013.

[11] T. Zhu, D. Wu, M. Liu, and D. W. Duan, "In-line fiber optic interferometric sensors in single-mode fibers," *Sensors (Basel)*, vol. 12, pp. 10430-49, 2012.

[12] L. H. Cho, C. Wu, C. Lu, and H. Y. Tam, "A Highly Sensitive and Low-Cost Sagnac Loop Based Pressure Sensor," *Sensors Journal, IEEE*, vol. 13, pp. 3073-3078, 2013.

[13] H. Y. Fu, H. Y. Tam, L. Y. Shao, X. Dong, P. K. Wai, C. Lu, *et al.*, "Pressure sensor realized with polarization-maintaining photonic crystal fiber-based Sagnac interferometer," *Appl Opt,* vol. 47, pp. 2835-9, May 20 2008.

[14] E. Van McKinney, *A Micheleson [i.e. Michelson] fiber optic pressure sensor with electro-optic feedback system for remote fluid pressure measurements*: University of Texas at Austin, 1991.

[15] H. G. Porte, V.; Kiryenko, S.; Goedgebuer, J. -P; Daniau, W.; Blind, P., "Imbalanced Mach-Zehnder interferometer integrated in micromachined silicon substrate for pressure sensor," *Lightwave Technology, Journal of* vol. 17, pp. 229-233, 1999.

[16] D. W. Stowe, D. R. Moore, and R. G. Priest, "Polarization Fading in Fiber Interferometric Sensors," *Microwave Theory and Techniques, IEEE Transactions on,* vol. 30, pp. 1632-1635, 1982.

[17] C. E. Lee and H. F. Taylor, "Sensor for smart structures based on the Fabry Perot interferometer," in *Fiber Optic Smart Structures,* E. Udd. ed New York: Wiley, 1995, pp. 249-269.

[18] T. Bae, R. A. Atkins, H. F. Taylor, and W. N. Gibler, "Interferometric Fiber-Optic Sensor Embedded in a Spark Plug for In-Cylinder Pressure Measurement in Engines," *Appl Opt,* vol. 42, pp. 1003-1007, 2003.

[19] M. J. Gander, W. N. Macpherson, J. S. Barton, R. L. Reuben, J. D. C. Jones, R. Stevens, *et al.*, "Embedded micromachined fibre optic Fabry-Perot pressure sensors in aerodynamics applications," *IEEE Sensors. J.*, vol. 3, pp. 102-107, 2003.

[20] J. J. Alcoz, C. E. Lee, and H. F. Taylor, "Embedded fiber-optic Fabry-Perot ultrasound sensor," *IEEE Trans Ultrason Ferroelectr Freq Control,* vol. 37, pp. 302-6, 1990.

[21] R. G. Minasamudram, "Optimization of wideband fiber optic hydrophone probe for ultrasound sensing applications," PhD, Drexel University, 2010.

[22] P. N. Wells, "Ultrasound imaging," *Phys Med Biol,* vol. 51, pp. R83-98, Jul 7 2006.

[23] Y. P. Wang, D. N. Wang, and W. Jin, "CO2 laser-grooved long period fiber grating temperature sensor system based on intensity modulation," *Appl Opt,* vol. 45, pp. 7966-70, Nov 1 2006.

[24] Y. P. Wang, L. Xiao, D. N. Wang, and W. Jin, "Highly sensitive long-period fiber-grating strain sensor with low temperature sensitivity," *Opt Lett,* vol. 31, pp. 3414-6, Dec 1 2006.

[25] W. Wang, N. Wu, Y. Tian, C. Niezrecki, and X. Wang, "Miniature all-silica optical fiber pressure sensor with an ultrathin uniform diaphragm," *Opt Express,* vol. 18, pp. 9006-14, Apr 26 2010.

[26] J. H. Chen, J. R. Zhao, X. G. Huang, and Z. J. Huang, "Extrinsic fiber-optic Fabry-Perot interferometer sensor for refractive index measurement of optical glass," *Appl Opt,* vol. 49, pp. 5592-6, Oct 10 2010.

[27] S. F. Correia, P. Antunes, E. Pecoraro, P. P. Lima, H. Varum, L. D. Carlos, *et al.*, "Optical fiber relative humidity sensor based on a FBG with a di-ureasil coating," *Sensors (Basel),* vol. 12, pp. 8847-60, 2012.

[28] F. Wang, X. Zhang, X. Wang, and H. Chen, "Distributed fiber strain and vibration sensor based on Brillouin optical time-domain reflectometry and polarization optical time-domain reflectometry," *Opt Lett,* vol. 38, pp. 2437-9, Jul 15 2013.

[29] C. Koch, "Measurement of ultrasonic pressure by heterodyne interferometry with a fiber-tip sensor," *Appl Opt,* vol. 38, pp. 2812-9, May 1 1999.

[30] M. D. Giovanni, *Flat and Corrugated Diaphragm Design Handbook*: Marcel Dekker, 1982.

[31] J. Xu, "High Temperature High Bandwidth Fiber Optic Pressure Sensors," PhD, Department of Electrical Engineering Virginia Polytechnic Institute and State University, Blacksburg, Virginia, 2005.

[32] D. J. Inman. Chapter 2 Response to Harmonic Excitation. Available: lcs3.syr.edu/faculty/glauser/mae321/.../004_Ch2-1_to_2-3.pdf

[33] D. G. Shombert, S. W. Smith, and G. R. Harris, "Angular response of miniature ultrasonic hydrophones," *Med. Phys.*, vol. 9, pp. 484-92, 1982.

[34] P. Morris, "A Fabry-Perot fibre-optic hydrophone for the characterisation of ultrasound fields," PhD, Department of Medical Physics and Bioengineering, University College London, 2008.

[35] J. F. Kruckler, A. Eisenberg, M. Krix, R. Lotsch, M. Pessel, and H. G. Trier, "Rigid piston approximation for computing the transfer function and angular response of a fiber-optic hydrophone," *J Acoust Soc Am,* vol. 107, pp. 1994-2003, Apr 2000.

[36] L. Song, "Detection and Position Location of Partial Discharges in Transformers Using Fiber Optic Sensors," M. S., Department of Electrical Engineering, Virginia Polytechnic Institute and State University, Blacksburg, Virginia, 2004.

[37] Z. Q. Zhao, J. M. K. MacAlpine, and M. S. Demokan, "Directional sensitivity of a fibre-optic sensor to acoustic signals in transformer oil," in *Advances in Power System Control, Operation and Management, 1997. APSCOM-97. Fourth International Conference on (Conf. Publ. No. 450)*, 1997, pp. 521-525 vol.2.

[38] L. Song, Z. Wang, K. Wang, and K. L. Cooper, "Angular Dependence of the Frequency Response of an Extrinsic Fabry–Pérot Interferometric (EFPI) Fiber Acoustic Sensor for Partial Discharge Detection," *Journal of Lightwave Technology*, vol. 24, pp. 2433-3438, 2006.

[39] P. R. Scheeper, W. Olthuis, and P. Bergveld, "The design, fabrication, and testing of corrugated silicon nitride diaphragms," *Microelectromechanical Systems, Journal of*, vol. 3, pp. 36-42, 1994.

[40] Q. Zou, Z. Wang, R. Lin, S. Yi, H. Gong, M. Lim, *et al.*, "A study on corrugated diaphragms for high-sensitivity structures," *J. Micromech. Microeng.*, vol. 7, pp. 82611-3, 1997.

[41] W. J. Wang, R. M. Lin, X. Li, and D. G. Guo, "Study of single deeply corrugated diaphragms for high-sensitivity microphones," *J. Micromech. Microeng.*, vol. 13, 184, 2003.

[42] A. Saran, D. C. Abeysinghe, and J. T. Boyd, "Microelectromechanical system pressure sensor integrated onto optical fiber by anodic bonding," *Appl Opt*, vol. 45, pp. 1737-42, Mar 10 2006.

[43] X. Wang, J. Xu, Y. Zhu, K. L. Cooper, and A. Wang, "All-fused-silica miniature optical fiber tip pressure sensor," *Opt Lett*, vol. 31, pp. 885-7, Apr 1 2006.

[44] E. Cibula and D. Donlagic, "Miniature fiber-optic pressure sensor with a polymer diaphragm," *Appl Opt*, vol. 44, pp. 2736-44, May 10 2005.

[45] S. Nesson, M. Yu, X. Zhang, and A. H. Hsieh, "Miniature fiber optic pressure sensor with composite polymer-metal diaphragm for intradiscal pressure measurements," *J Biomed Opt*, vol. 13, pp. 044040, Jul-Aug 2008.

[46] T. T. Fernandez, S. M. Eaton, G. Della Valle, R. M. Vazquez, M. Irannejad, G. Jose, *et al.*, "Femtosecond laser written optical waveguide amplifier in phospho-tellurite glass," *Opt Express*, vol. 18, pp. 20289-97, Sep 13 2010.

[47] S. L. Li, P. Han, M. Shi, Y. Yao, B. Hu, M. Wang, *et al.*, "Low-loss channel optical waveguide fabrication in Nd(3+)-doped silicate glasses by femtosecond laser direct writing," *Opt Express,* vol. 19, pp. 23958-64, Nov 21 2011.

[48] J. Yong, F. Chen, Q. Yang, G. Du, H. Bian, D. Zhang, *et al.*, "Rapid Fabrication of Large-Area Concave Microlens Arrays on PDMS by a Femtosecond Laser," *ACS Appl Mater Interfaces,* vol. 5, pp. 9382-9385, Oct 9 2013.

[49] T. Meunier, A. B. Villafranca, R. Bhardwaj, and A. Weck, "Fabrication of microlens arrays in polycarbonate with nanojoule energy femtosecond laser pulses," *Opt Lett,* vol. 37, pp. 4266-8, Oct 15 2012.

[50] X. Fang, C. R. Liao, and D. N. Wang, "Femtosecond laser fabricated fiber Bragg grating in microfiber for refractive index sensing," *Opt Lett,* vol. 35, pp. 1007-9, Apr 1 2010.

[51] T. Geernaert, K. Kalli, C. Koutsides, M. Komodromos, T. Nasilowski, W. Urbanczyk, *et al.*, "Point-by-point fiber Bragg grating inscription in free-standing step-index and photonic crystal fibers using near-IR femtosecond laser," *Opt Lett,* vol. 35, pp. 1647-9, May 15 2010.

[52] T. Wei, Y. Han, H. L. Tsai, and H. Xiao, "Miniaturized fiber inline Fabry-Perot interferometer fabricated with a femtosecond laser," *Opt Lett,* vol. 33, pp. 536-8, Mar 15 2008.

[53] C. R. Liao, T. Y. Hu, and D. N. Wang, "Optical fiber Fabry-Perot interferometer cavity fabricated by femtosecond laser micromachining and fusion splicing for refractive index sensing," *Opt Express,* vol. 20, pp. 22813-8, Sep 24 2012.

[54] L. Yuan, T. Wei, Q. Han, H. Wang, J. Huang, L. Jiang, *et al.*, "Fiber inline Michelson interferometer fabricated by a femtosecond laser," *Opt Lett,* vol. 37, pp. 4489-91, Nov 1 2012.

[55] I. Coherent. (2013). Available: http://www.coherent.com/products/?940/RegA

[56] Y. Zhang, J. Huang, X. Lan, L. Yuan, A. Kaur, and H. Xiao, "High temperature fiber optic Fabry-Perot interferometric pressure sensor fabricated by femtosecond laser," *Opt. Letters,* vol. 38, pp. 4609-4612, Nov 15 2013.

[57] T. Wei, "High temperature tolerant optical inline fiber sensors by laser fabrication," PhD, Department of Electrical and Computer Engineering, Missouri University of Science and Technology, Rolla, MO, 2010.

[58] Y. Huang, T. Wei, Z. Zhou, Y. Zhang, G. Chen, and H. Xiao, "An extrinsic Fabry–Perot interferometer-based large strain sensor with high resolution," *Meas. Sci. Technol.,* vol. 21, pp. 105308, 2010.

[59] X. Lan, Y. Han, T. Wei, Y. Zhang, L. Jiang, H. L. Tsai, *et al.*, "Surface-enhanced Raman-scattering fiber probe fabricated by femtosecond laser," *Opt Lett,* vol. 34, pp. 2285-7, Aug 1 2009.

[60] D. Koutsoyiannis, "Clausius–Clapeyron equation and saturation vapour pressure: simple theory reconciled with practice," *Eur. J. Phys,* vol. 33, pp. 295-305, 2012.

[61] B. T. labratory, *Transmission Systems for Communications*, 3rd Edition ed. NC: Western Electric Co., 1985.

[62] G. Fusiek, P. Niewczas, and J. R. McDonald, "Design of a highly accurate optical sensor system for pressure and temperature monitoring in oil wells," presented at the Instrumentation and Measurement Technology Conference, 2009. I2MTC '09. IEEE, Singapore, 2009.

[63] A. Sun, X. Q. Qiao, A. Jia, M. Li, and D. Z. Zhao, "Study of simultaneous measurement of temperature and pressure using double fiber Bragg gratings with polymer package," *Opt. Eng.* , vol. 44, pp. 034402-034402-4, 2005.

[64] Y. Liu, Z. Guo, Y. Zhang, K. S. Qiang, and X. Dong, "Simultaneous pressure and temperature measurement with polymer-coated fiber Bragg grating," *Electr. Lett.*, vol. 36, pp. 564-566, 2000.

[65] P. Kumar, M. V. Rajashekhar, and S. K. Ghorai, "Multi-parameter sensing system using sampled fiber Bragg grating," presented at the International conference on Optics and Photonics, Chandigarh, India, 2009.

[66] S. Zheng and X. Zhang, "Simultaneous Measurement of Pressure and Temperature Using a Single Fiber Bragg Grating," presented at the Progress In Electromagnetics Research Symposium, Hangzhou, 2005.

[67] K. Bremer, E. Lewis, B. Moss, G. Leen, S. Lochmann, and I. Mueller, "Conception and preliminary evaluation of an optical fibre sensor for simultaneous measurement of pressure and temperature," in *J. Phys.: Conf. Ser.*, Edinburgh, UK, 2009, p. 012016.

[68] S. H. Aref, H. Latifi, M. I. Ziabii, and M. Afshari, "Fiber optic Fabry–Perot pressure sensor with low sensitivity to temperature changes for downhole application," *Opt. Commun,* vol. 269, pp. 322-330, 2007.

[69] Y. L. Wang, C. L. Yang, H. Y. C. Jan, G. R. Lin, J. C. Mau, M. Y. Fu, *et al.*, "Simultaneous temperature and pressure measurement using a packaged FBG and LPG," in *OptoeElectronics and Communications Conference (OECC), 2010 15th*, Sapporo, 2010, pp. 814-815.

[70] C. Wu, Y. Zhang, and B. Guan, "Simultaneous Measurement of Temperature and Hydrostatic Pressure Using Bragg Gratings in Standard and Grapefruit Microstructured Fibers," *IEEE Sens. J.,* vol. 11, pp. 489-492, 2011.

[71] S. Pevec and D. Donlagic, "Miniature all-fiber Fabry-Perot sensor for simultaneous measurement of pressure and temperature," *Appl Opt,* vol. 51, pp. 4536-41, Jul 1 2012.

[72] S. Takahashi and S. Shibata, "Thermal variation of attenuation for optical fibers," *J. Non-Cryst. Solids* vol. 30, pp. 359-370, 1979.

[73] W. Wang, J. Wen, F. Pang, N. Chen, and T. Wang, "All single mode fiber Fabry Perot interferometric high temperature fabricated with femtosecond laser," *Chin J Lasers,* vol. 39, pp. 1005001, 2012.

[74] T. Wei, X. Lan, and H. Xiao, "Fiber Inline Core–Cladding-Mode Mach–Zehnder Interferometer Fabricated by Two-Point CO2 Laser Irradiations," *IEEE Photonic Tech. L.,* vol. 21, pp. 669-671, 2009.

[75] W. Wang, D. Ding, N. Chen, and F. Pang, "Quasi-Distributed IFPI Sensing System Demultiplexed With FFT-Based Wavelength Tracking Method," *IEEE Sens. J.,* vol. 12, pp. 2875-2880, 2012.

VITA

Yinan Zhang was born on February 18, 1987 in Anhui, China. In June 2008, she obtained a bachelor's degree in Department of Instrument Science and Opto-Electronic Engineering from Beijing University of Aeronautics and Astronautics, Beijing, China. In August 2008, she enrolled at Missouri University of Science and Technology to pursue a master's degree in Department of Electrical and Computer Engineering under the guidance of Dr. Hai Xiao. She received her Master of Science Degree in Electrical Engineering in May 2010. Then she continued her study towards a doctoral degree in Department of Electrical and Computer Engineering under the guidance of Dr. Hai Xiao. In Dec 2013, she received her Ph.D in Electrical Engineering from Missouri University of Science and Technology. During her graduate study, she authored and co-authored 12 journal and conference papers. She reviewed 6 papers for Journal of Micromechanics & Micro-engineering, IEEE sensors journal, IEEE Transactions on Measurement & Instrumentation and Chinese optics letters. She is a student member of OSA, IEEE and SPIE.